THE JOURNAL OF BIOLOGICAL CHEMISTRY VOL. 290, NO. 33, pp. 20541–20555, August 14, 2015
© 2015 by The American Society for Biochemistry and Molecular Biology, Inc. Published in the U.S.A.

The Cerebro-oculo-facio-skeletal Syndrome Point Mutation F231L in the ERCC1 DNA Repair Protein Causes Dissociation of the ERCC1-XPF Complex*

Received for publication, January 22, 2015, and in revised form, June 16, 2015 Published, JBC Papers in Press, June 16, 2015, DOI 10.1074/jbc.M114.635169

Maryam Faridounnia[‡], Hans Wienk[‡], Lidija Kovačič[§1], Gert E. Folkers[‡], Nicolaas G. J. Jaspers[¶], Robert Kaptein[‡], Jan H. J. Hoeijmakers[¶], and Rolf Boelens[‡2]

From the [‡]Bijvoet Center for Biomolecular Research, Utrecht University, Padualaan 8, 3584 CH Utrecht, The Netherlands, the [§]Department of Molecular and Biomedical Sciences, Jožef Stefan Institute, Jamova cesta 39, SI-1000 Ljubljana, Slovenia, and the [¶]Department of Genetics, Erasmus Medical Center, PO Box 2040, 3000 CA Rotterdam, The Netherlands

Background: An F231L mutation in the DNA repair complex ERCC1-XPF causes severe disorders.
Results: The observed enhanced dissociation of the mutant ERCC1-XPF helix-hairpin-helix dimer relates to an altered orientation for the interaction anchor Phe^{894} of XPF near Phe^{231} of ERCC1.
Conclusion: The local structure around Phe^{231} is essential for complex stability.
Significance: Studying mutations interfering with DNA repair is crucial to understand endonuclease-related diseases.

The ERCC1-XPF heterodimer, a structure-specific DNA endonuclease, is best known for its function in the nucleotide excision repair (NER) pathway. The ERCC1 point mutation F231L, located at the hydrophobic interaction interface of ERCC1 (excision repair cross-complementation group 1) and XPF (xeroderma pigmentosum complementation group F), leads to severe NER pathway deficiencies. Here, we analyze biophysical properties and report the NMR structure of the complex of the C-terminal tandem helix-hairpin-helix domains of ERCC1-XPF that contains this mutation. The structures of wild type and the F231L mutant are very similar. The F231L mutation results in only a small disturbance of the ERCC1-XPF interface, where, in contrast to Phe^{231}, Leu^{231} lacks interactions stabilizing the ERCC1-XPF complex. One of the two anchor points is severely distorted, and this results in a more dynamic complex, causing reduced stability and an increased dissociation rate of the mutant complex as compared with wild type. These data provide a biophysical explanation for the severe NER deficiencies caused by this mutation.

UV light, ionizing radiation, mutagenic compounds, and natural cellular metabolism can damage DNA and lead to mutations causing cancer or cell death and senescence contributing to aging-related disorders (1). As a countermeasure, the cell has developed a set of complementary repair mechanisms, one of which is the nucleotide excision repair (NER)[3] pathway (2, 3). This multistep "cut-and-patch" repair system deals with the broad class of helix-distorting lesions, including UV-induced DNA lesions and numerous bulky chemical adducts and intrastrand cross-links. Two proteins involved in this repair process, ERCC1 (excision repair cross-complementation group 1) and XPF (xeroderma pigmentosum complementation group F) form a heterodimeric complex that functions as a structure-specific DNA endonuclease responsible for the 5′ incision when the lesion is excised from the DNA as a 22–30 oligonucleotide in a late step of the NER reaction (4, 5). There is considerable evidence for additional NER-independent roles of the ERCC1-XPF heterodimer in homologous recombination (6–9), repair of interstrand DNA cross-links (9, 10), telomere length maintenance (11–13), double strand break repair (14), and gene conversion (9, 15).

The proper functioning of the ERCC1-XPF complex as an endonuclease in NER critically depends on the formation of a heterodimer via the proteins' C-terminal tandem helix-hairpin-helix $(HhH)_2$ domains (16–19). This contact region of the dimer is not only important for the interaction between the monomers but also plays a role in DNA binding; the C-terminal domain of ERCC1 is essential for double-stranded DNA (dsDNA) binding (18, 20, 21), whereas the C-terminal $(HhH)_2$ domain of XPF can bind single-stranded DNA (ssDNA) (22). We proposed that this would position the ERCC1-XPF complex at an ss/dsDNA junction and place the catalytic module of

* This research was supported by the Netherlands Foundation of Chemical Research (NWO-CW) and the European Union (Project BioNMR, No. 261863); the Royal Academy of Arts and Sciences of the Netherlands (academic professorship to J. H. J. H.); the European Research Council (Project DamAge No. GA233424; to J. H. J. H.); and the Slovenian Ministry of Higher Education, Science, and Technology (Z1-4071; to L. K.) and their support of the Infrastructural Centre for Analysis of Molecular Interactions, Department of Biology, Biotechnical Faculty, University of Ljubljana, Slovenia. The authors declare that they have no conflicts of interest with the contents of this article.

The atomic coordinates and structure factors (code 2MUT) have been deposited in the Protein Data Bank (http://wwpdb.org/).

NMR data for the mutant F231L ERCC1-XPF $(HhH)_2$ heterodimer have been deposited in the BioMagResBank database (http://www.bmrb.wisc.edu) under accession number 25232.

[1] Present address: School of Medicine and Medical Science, Conway Institute of Biomolecular and Biomedical Research, University College Dublin, Dublin 4, Ireland.

[2] To whom correspondence should be addressed. Tel.: 31-30-2534035; Fax: 321-30-2537623; E-mail: r.boelens@uu.nl.

[3] The abbreviations used are: NER, nucleotide excision repair; HhH, helix-hairpin-helix; HSQC, heteronuclear single quantum coherence; SPR, surface plasmon resonance; NTA, nitrilotriacetic acid; CLEANEX-PM, phase-modulated clean chemical exchange.

Downloaded from http://www.jbc.org/ at Universiteitsbibliotheek Utrecht on December 3, 2015

XPF, which is adjacent to its $(HhH)_2$ domain, at the 5′ site at some distance from the DNA lesion (22).

In classic cases of XPF deficiency, the DNA repair function is still partly retained, and UV sensitivity is only moderately increased (23–25). In recent years, however, several more severe cases of XPF-related deficiencies have been described (10, 26–29). For instance, it was shown that mutations in XPF can cause Fanconi anemia (29). Mutational studies on a mouse homolog of human ERCC1 have shown the N terminus of ERCC1, despite being dispensable for DNA repair, to be important for heterodimer expression (7, 30). Inherited deficiencies in ERCC1 are rare in humans (28, 31, 32), probably reflecting the lethality of many genetic mutations in this protein, which became apparent also from studies in mice perinatal mortality (33). The similarity of these symptoms to those resulting from XPF defects in mice, combined with the biochemical and cellular parallels, supports the notion that ERCC1 and XPF function as an obligate complex *in vivo*. Only two cases involving ERCC1 defects have been reported in humans, having in common a F231L point mutation that causes one of the severest cases of NER deficiency known until now. One case (*165TOR*) is a biallelic heterozygous mutation, one of which is F231L, which leads to severe degeneration of the brain and spinal cord, diagnosed as cerebro-oculo-facio-skeletal syndrome, and death at early infancy (31, 34). The other case of ERCC1 deficiency is a biallelic homozygous F231L mutation, resulting in an early onset of Cockayne syndrome and the patient's death at early infancy. Both cases link the F231L mutation to NER deficiency, where the ERCC1-XPF complex is still present, but in reduced quantities, resulting in slower repair rates (28, 31).

Phe^{231} is conserved in ERCC1 of invertebrates and mammals. The residue is located in the C-terminal $(HhH)_2$ domain of ERCC1, and in the wild type protein structure, it has extensive interactions with the $(HhH)_2$ domain of XPF (16, 18, 20, 21). Therefore, in principle, the loss of ERCC1-XPF functionality in the F231L mutant could be due to ERCC1 instability and/or the reduced stability of the entire ERCC1-XPF complex. Furthermore, because the phenylalanine is in close proximity to the hairpin regions of the ERCC1 $(HhH)_2$ domain that are important for its DNA binding role, the mutation could also affect the DNA binding properties of the ERCC1-XPF complex. In order to explore these possibilities, we produced and purified the ERCC1-XPF $(HhH)_2$ complex containing the F231L mutation and compared several structural and functional properties with those of wild type ERCC1-XPF. We show that whereas the mutant heterodimer preserves the overall fold of the ERCC1-XPF $(HhH)_2$ complex as well as its DNA binding properties, the mutation causes a side chain reorientation for residue 231 that disrupts interactions with nearby amino acids of XPF. We show that this small, local disturbance in the ERCC1-XPF heterodimer leads to a lower stability of the complex due to an increased dissociation rate.

Experimental Procedures

Cloning, Protein Expression, and Purification—The construct for the F231L ERCC1 $(HhH)_2$ mutant was prepared by using an extended mutagenic 5′ primer during PCR amplification with the wild type construct as a template. Subsequently, F231L ERCC1 was cloned into the BamHI-XhoI site of the pET28b bicistronic expression vector (18), substituting the wild type ERCC1 coding region. The construction was verified by DNA sequencing. The final construct consists of F231L ERCC1(220–297), followed by a C-terminal flexible linker and His_6 tag GGLEHHHHHH, and XPF(823–905). The plasmid was transformed into the *Escherichia coli* Rosetta (DE3) strain, overexpressed, and purified using an Ni^{2+}-nitrilotriacetic acid (NTA)-agarose column, followed by gel filtration as described for wild type ERCC1-XPF (18). During NMR analysis, it was found that the expressed protein was a 1:1 mixture with a longer than expected protein, probably due to the presence of a rare alternate start codon (35, 36) next to the constructed one, which resulted in seven additional amino acids at the N terminus of ERCC1 (RIRRRYN). This alternative initiation codon was present in both wild type and mutant and did not interfere with DNA binding or heterodimer stability as judged by NMR.

Surface Plasmon Resonance—DNA binding to the F231L ERCC1-XPF $(HhH)_2$ heterodimer was measured by surface plasmon resonance (SPR) as described before (37). All solutions for SPR were filtered through a 0.22-μm filter and degassed. The experiments were performed at 12 °C in 10 mM Hepes, pH 7.5, 50 mM NaCl, and 0.005% (w/v) Tween 20 (SPR buffer) at 10 μl/min using a Biacore® X system (Biacore AB, Uppsala, Sweden). The mutant and wild type ERCC1-XPF $(HhH)_2$ complexes were exchanged to the SPR buffer using Zeba Spin Desalting Columns (Thermo Scientific). Protein concentrations were determined by UV spectroscopy using a Nanodrop instrument (Thermo Scientific) assuming $\epsilon_{280} = 2980\ mM^{-1}\ cm^{-1}$. At low concentrations, it was additionally estimated using SDS-PAGE. Low binding tubes and tips were used to prevent the loss of sample during handling. Mutant or wild type ERCC1-XPF $(HhH)_2$ complex (0.05 μM), in the absence or presence of double strand "bubble10" (*i.e.* annealed DNA GGGCGGCGGGT$_{10}$GGCGGGGCGG and CCCGCCGCCCT$_{10}$CCGCCCCGCC) with concentrations ranging from 0.01 to 100 μM using a dilution factor of 2, was incubated in the SPR buffer for 20 min on ice and injected over the NTA CM5 sensor chip. DNA association was monitored for 60 s, and the dissociation was monitored for 120 s. Before each SPR experiment, Ni^{2+} was immobilized on the second flow cell of the sensor chip (Biacore AB) while the first flow cell was used as a reference surface. Between consecutive injections, the chip was regenerated with 10 μl of 0.25 M EDTA in 3.5 M guanidine, pH 8.0. Data were processed using Biaevaluation version 3.2 software. To calculate the apparent dissociation constant (K_d^{app}) of the DNA binding to the ERCC1-XPF $(HhH)_2$ heterodimer, the relative amount of DNA-free protein was divided by the total DNA concentration and fitted according to a simple 1:1 binding model using the software Prism (GraphPad Software Inc.). Because the DNA prevented His tag binding of the ERCC1-XPF $(HhH)_2$ domains on the Ni^{2+}-NTA surface, the relative amount of DNA-free protein was determined as response values at the end of the loading time of 60 s (R_{60}) divided by the R_{60} value of the ERCC1-XPF $(HhH)_2$ heterodimer in the absence of DNA (fraction = $R_{60}[\text{ERCC1-XPF}]_{free}/R_{60}[\text{ERCC1-XPF}]_{total}$).

The real-time monitoring of the interaction of ERCC1 with XPF was performed in a flow cell maintaining the laminar flow

Downloaded from http://www.jbc.org/ at Universiteitsbibliotheek Utrecht on December 3, 2015

(Biacore AB) and with a Sensor Chip Ni^{2+}-NTA (Biacore AB) (37). All experiments were performed at a flow rate of 20 μl/min in an SPR buffer containing 50 or 150 mM NaCl. A set of experiments was conducted at three concentrations of wild type and mutant ERCC1-XPF $(HhH)_2$ heterodimer (0.2, 0.1, and 0.05 μM) and three temperatures (12, 20, and 25 °C). Each experiment was executed twice. The association of the ERCC1-XPF complex on the chip and the dissociation from the chip (expressed as the reciprocal of time) was monitored for 60 and 120 s, respectively. Identical amounts of proteins were loaded on the chip without preloaded Ni^{2+} in order to subtract the baseline from each obtained sensogram before analysis. SPR curves were fitted as a single-phase decay model over 60–180 s using the software GraphPad Prism using the following equation.

$$R = (R_0 - P) \times e^{(-k_{off}^{app} \times t)} + P \quad \text{(Eq. 1)}$$

Here, R is the response in arbitrary response units, R_0 is the maximum response after association (60 s), P is the plateau at infinite times, and k_{off}^{app} is the sum of the off-rate of the XPF dissociation from His-tagged ERCC1 and of the His-tagged protein from the chip. The SPR chip performance was optimized using different protein concentrations combined with different Ni^{2+} concentrations and different flow rates, based on the findings of Nieba *et al.* (37). The protein complex was loaded on the chip with a 12–25 °C temperature gradient, and the dissociation was followed for 1000 s. No reliable data could be obtained above 25 °C due to elevated dissociation of His-tagged protein from the chip. The baseline for the buffer was subtracted.

Circular Dichroism—CD spectra were measured using a JASCO J-810 spectropolarimeter as described before (38, 39). The thermal unfolding of wild type and mutant ERCC1-XPF-His_6 was measured in the far-UV wavelength range (190–250 nm) under identical conditions (CD buffer: 50 mM $NaPO_4$, 100 mM NaCl, pH 7.0; protein concentrations, about 25 μM; cell path length, 1 mm). Ten 10-s scans were recorded, and the temperature was increased from 15 to 85 °C in increments of 1 °C/min. The signal intensities at 222 nm were collected for each temperature and analyzed as described previously (38).

Thermal Shift Assay—Thermal shift experiments were performed in 96-well thin wall PCR plates sealed with optical-quality sealing tape. The presented transition temperatures are the averages of three independent experiments performed at different protein concentrations. Each sample contained 5 μg of protein in 25 μl of buffer containing 2.5 μl of 100× diluted Sypro Orange (Molecular Probes, Life Technologies, Inc.). The fluorescence changes were followed on an iCycler iQ PCR detection system (Bio-Rad) from 15 to 95 °C in increments of 0.2 °C/min by monitoring Sypro Orange fluorescence and analyzed (40). The wavelengths used for excitation and emission were 490 and 575 nm, respectively.

NMR Spectroscopy—NMR spectra were recorded at 290 K, unless indicated differently, using a Bruker Avance DRX 600-MHz system with a TCI cryoprobe, an Avance II 750-MHz machine with a TXI probe, and an Avance III 900-MHz spectrometer with a TCI cryoprobe. Triple resonance experiments (including HMCMCGCBCACONH) were recorded using 0.4 mM $^{13}C/^{15}N$-labeled ERCC1-XPF-His_6 in NMR buffer (50 mM NaP_i, 100 mM NaCl, 8% ^2H_2O, pH 7.0) (41, 42). Spectra were processed with Topspin version 2.1/3.0, or NMRPipe (43) and analyzed in Sparky (44) to assign backbone and side-chain ^1H, ^{15}N, and ^{13}C resonances. A two-dimensional NOE spectrum (τ_{mix} = 80 ms), a three-dimensional NOESY-$^1H,^{15}N$ HSQC spectrum (τ_{mix} = 100 ms), and a three-dimensional NOESY-$^1H,^{13}C$ HSQC spectrum (τ_{mix} = 80 ms) were recorded. An additional three-dimensional NOESY-$^1H,^{13}C$ HSQC spectrum (τ_{mix} = 80 ms) was obtained with ERCC1-XPF in D_2O.

For NMR temperature series, two-dimensional $^1H,^{15}N$ HSQC spectra were measured at temperatures ranging from 280 to 333 K using 400 μM ^{15}N-labeled wild type and mutant ERCC1-XPF in NMR buffer. In total, 15 two-dimensional $^1H,^{15}N$ HSQC spectra were recorded at 750 MHz, and chemical shift changes were analyzed as described before (45, 46).

Proton-deuterium exchange of ^{15}N-labeled mutant and wild type ERCC1-XPF $(HhH)_2$ heterodimer was measured at 750 MHz in 100 mM NaCl, 50 mM NaP_i, pH 6.8 (meter reading) in D_2O. Prior to monitoring H/D exchange, the acquisition parameters were adjusted with wild type ERCC1-XPF prepared in NMR buffer (47). Dissolving the lyophilized sample in ^2H_2O, transferring to the NMR tube, transfer to the NMR instrument, and temperature equilibration resulted in a total preparation time of 8 min. Thereafter, the acquisition of series of two-dimensional $^1H,^{15}N$ HSQC spectra for following the H/D exchange was started. For each residue, the decay of the signal intensities as a function of time was evaluated as described previously (48).

Phase-modulated clean chemical exchange (CLEANEX-PM) experiments were recorded at 600 MHz as explained by Hwang *et al.* (49). Signal intensities were obtained from two-dimensional (CLEANEX-PM)-fast HSQC spectra recorded with a mixing time of 100 ms and for reference compared with a control fast HSQC spectrum as described previously (41).

NMR structures were calculated using CYANA version 3.0 (50, 51). Distance restraints were derived from NOESY peak intensities. Torsion angle restraints φ and ψ were derived from H^N, Hα, ^{15}N, $^{13}C\alpha$, $^{13}C\beta$, and ^{13}CO chemical shifts using TALOS+ (52, 53) with an extra error of ±10°. In each CYANA cycle, 100 structures were generated and energy-minimized using 10,000 steps of simulated annealing. After initial CYANA runs, additional NOE assignments were obtained by manual inspection of the NOESY spectra. Before water refinement, CYANA-derived NOE and hydrogen bond restraints, in addition to the torsion angle restraints derived from TALOS+ (52, 53), were used to calculate 100 structures with CNS (54, 55). Each of these structures was subsequently refined in explicit water using restrained molecular dynamics using the RECOORD protocol (55). The 20 lowest energy conformations were validated using WHATIF, WHATCHECK, and iCing (56–58). Molecular images were generated using PyMOL (59, 60).

For the wild type ERCC1-XPF $(HhH)_2$ heterodimer domain, we observed inconsistencies in the precise length of helix α. Whereas the helix length for the F231L ERCC1-XPF mutant was consistent with that of the crystal structure of wild type ERCC1-XPF (Protein Data Bank code 2A1J), this helix was

Downloaded from http://www.jbc.org/ at Universiteitsbibliotheek Utrecht on December 3, 2015

shorter in the NMR structure of wild type ERCC1-XPF (Protein Data Bank code 1Z00). Therefore, the NMR structure of wild type ERCC1-XPF was recalculated following the same protocol as for the mutant. For this, the previously determined NOE-based restraints and restraints for hydrogen bonds (18) were combined with φ and ψ torsion angle restraints derived from TALOS+ (52, 53) for the calculation of an ensemble of 100 conformers with CNS (54, 55). Water refinement, validation, and generation of molecular images were as for F231L ERCC1-XPF.

Results

Similar to the heterodimeric complex of the C-terminal $(HhH)_2$ domains of wild type ERCC1-XPF (18), the system containing the F231L mutation could only be overexpressed and purified as an obligate complex using a bicistronic expression vector. During size exclusion chromatography, there was no indication of dissociation, arguing that F231L ERCC1-XPF can form a stable heterodimeric $(HhH)_2$ complex, similar to the wild type situation.

DNA Binding—In wild type ERCC1, the helices of the first HhH motif make extensive contacts with the dsDNA minor groove near the ss/dsDNA junction (22). Therefore, the F231L mutation, located in this first helix, could well interfere with DNA binding of ERCC1-XPF. It is known that bubble-shaped DNA substrates containing ss/dsDNA junctions efficiently bind wild type ERCC1-XPF heterodimer (18, 21). One of the highest affinity DNA probes appears to be "bubble10," where two double-stranded GC-rich segments flank a region of 10 unpaired thymine bases. Using an electrophoretic mobility shift assay (EMSA), we found that both wild type and F231L mutant ERCC1-XPF bind to DNA with comparable affinity (data not shown). However, we found that the relatively weak DNA binding of ERCC1-XPF can be more accurately analyzed using SPR. For the immobilization of the ERCC1-XPF complex to the sensor chip, we made use of the His-tagged ERCC1, because alternative coupling techniques using present protein cysteines, lysines, or the N terminus could lead to random orientation of the complex on the chip or interference with DNA binding. We have compared the ability of F231L and wild type ERCC1-XPF to bind bubble10 DNA. For this, wild type or mutant heterodimer were immobilized on Ni^{2+}-NTA chips via the C-terminal Histidine-tag of ERCC1 followed by loading of bubble10 DNA. The addition of bubble10 DNA caused dissociation of the heterodimer from the chip, which allowed to determine the fraction of free heterodimer as a function of the DNA concentration. The recorded SPR responses (Fig. 1, *A* and *B*) of wild type and mutant complexes upon DNA binding were subsequently used to calculate the dissociation constants (K_d), as described in detail under "Experimental Procedures." Both were determined to be about 0.2 μM (*i.e.* within error the same) (Fig. 1*C*). These DNA binding studies show that impaired DNA binding cannot be the explanation for the malfunctioning of nucleotide excision repair as seen for the patients with the ERCC1-XPF F231L mutation.

Biophysical Characterization—Next, the effect of the F231L mutation on the stability of the ERCC1-XPF $(HhH)_2$ complex was analyzed. We compared the temperature-dependent behavior of F231L and wild type ERCC1-XPF $(HhH)_2$ heterodimers using a thermal shift assay (ThermoFluor) (40), which measures the increase in Sypro Orange fluorescence upon exposure of hydrophobic patches during protein unfolding. The assay is commonly used to follow the unfolding of a protein with increasing temperatures, but it can also probe the dissociation of a protein complex. Previously, we studied the temperature stability of wild type ERCC1-XPF and homodimer $(XPF)_2$ using CD spectroscopy (38). In these studies, we found that ERCC1 dissociates from ERCC1-XPF and unfolds at a temperature of ~50 °C and that at the same time, XPF converts into a homodimeric $(XPF)_2$. Subsequently, by further increasing the temperature, the $(XPF)_2$ homodimer unfolds at ~75 °C. In the ThermoFluor experiment of ERCC1-XPF, also two transitions upon temperature increase were found (Fig. 1*D*), similar to what was observed previously using CD spectroscopy (38). As before, the first transition at ~50 °C is interpreted as the dissociation of the ERCC1-XPF heterodimer followed by ERCC1 denaturation, and the second transition at ~75 °C is explained as the unfolding of subsequently formed XPF homodimers. However, we noted a significant difference in the first transition temperatures between the wild type and F231L complexes, with onsets of dissociation at 52.0 ± 0.5 and 47.5 ± 1.0 °C, respectively. Although the difference in transition temperatures for the heterodimers can be interpreted as directly caused by a difference in unfolding of mutant *versus* wild type ERCC1-XPF, it could also be the result of structural distortions in ERCC1, in its binding partner XPF, and/or by enhanced dissociation of ERCC1-XPF, which could all lead to increased exposure of hydrophobic surfaces.

Far-UV circular dichroism (CD) directly probes changes in secondary structure formation, and ellipticity at 222 nm is indicative for the helical content of proteins (61). For both mutant and wild type ERCC1-XPF, again a biphasic behavior was observed upon increasing temperature, similarly as previously observed for the wild type heterodimer (Fig. 1*E*) (38). Also here, the first transition (at a T_m of 51.0 ± 1.0 °C) reflects heterodimer dissociation followed by ERCC1 $(HhH)_2$ unfolding, whereas the XPF $(HhH)_2$ domain remains folded and forms a homodimer (38). The high temperature transition (with a T^m of 76.0 ± 1.0 °C) reflects XPF homodimer dissociation and subsequent unfolding. Comparing the change in ellipticity as a function of temperature for the F231L and wild type ERCC1-XPF complex, we observe no evident differences in the first transition between the two proteins. The second transition is also very similar for both complexes, which can be expected because in both cases it probably involves the unfolding of the same XPF homodimer. Whereas the CD spectra show that the ERCC1 and XPF secondary structure elements of both wild type and mutant ERCC1-XPF start to unfold at similar temperatures, the ThermoFluor analysis shows that the mutant heterodimer is influenced already at lower temperature than wild type. Because CD monitors the unfolding of helices, whereas the ThermoFluor analysis can also signal dissociation of the heterodimer that precedes the unfolding of the ERCC1 monomer, the observed differences are indicative for the increased dissociation of ERCC1-XPF $(HhH)_2$ heterodimers because of the F231L mutation.

Downloaded from http://www.jbc.org/ at Universiteitsbibliotheek Utrecht on December 3, 2015

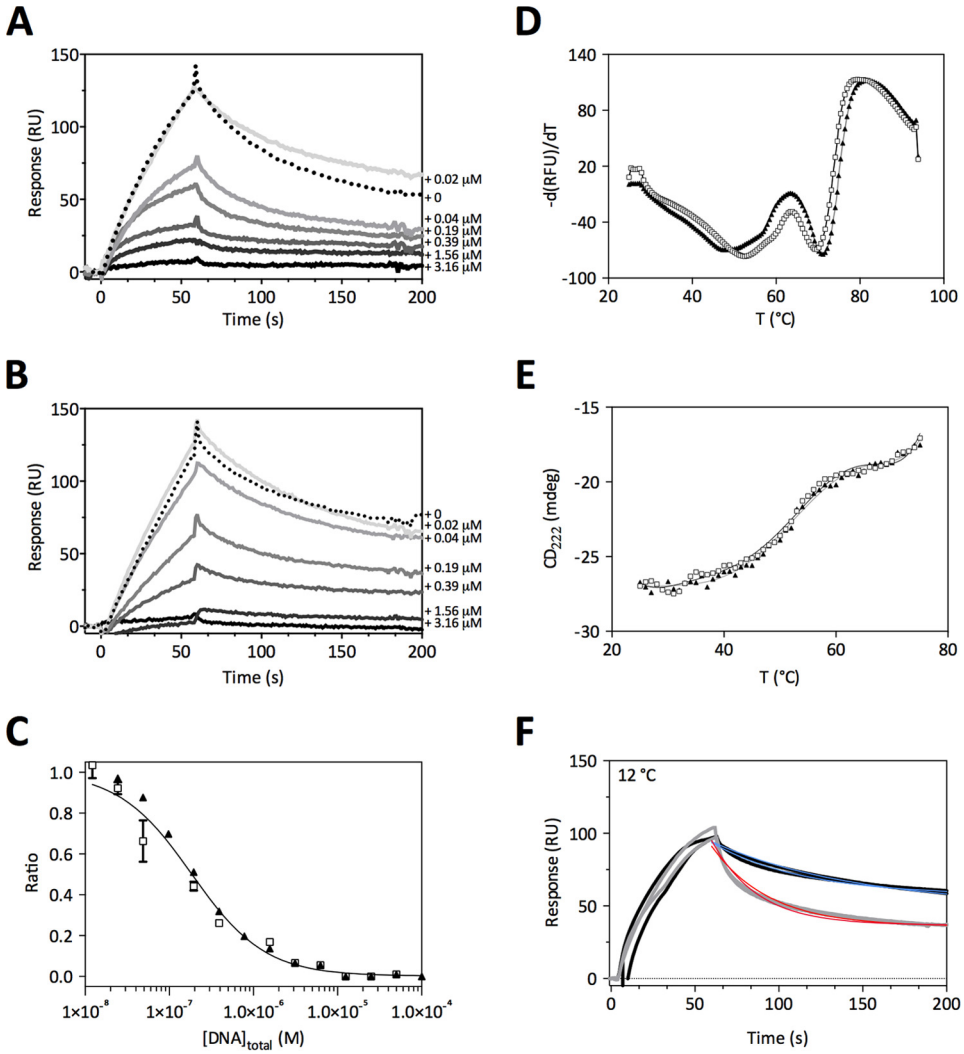

FIGURE 1. **DNA binding and stability of the wild type and F231L ERCC1-XPF $(HhH)_2$ heterodimers.** *A*, SPR with different concentrations of bubble10 DNA binding to the wild type ERCC1-XPF $(HhH)_2$ heterodimer. *B*, same as *A* but for the mutant F231L ERCC1-XPF $(HhH)_2$ complex. *C*, DNA binding curves of wild type (□) and mutant (▲) ERCC1-XPF based upon the SPR data from *A* and *B*. The figure displays the ratio R_{60}[ERCC1-XPF]$_{free}$/R_{60}[ERCC1-XPF]$_{total}$ as a function of the concentration of bubble10 DNA. *D*, thermal shift assay for wild type (□, *black line*) and mutant (▲, *gray line*) ERCC1-XPF. The stability of ERCC1-XPF $(HhH)_2$ is measured using the Sypro Orange Thermofluor assay (40). Note that the concentration of mutant ERCC1-XPF and thus also XPF homodimer was slightly higher than that of wild type, causing an apparent higher transition temperature for XPF homodimer at ~75 °C. *E*, thermal stability of wild type (□) and mutant (▲) ERCC1-XPF measured by CD spectroscopy. *F*, dissociation of ERCC1-XPF measured by SPR at 150 mM NaCl and 12 °C. The graphs show the dissociation of XPF from immobilized wild type ERCC1 (data in *black*, fit in *blue*) and immobilized F231L ERCC1 (data in *gray*, fit in *red*). *RU*, arbitrary response units.

Association and dissociation of proteins forming complexes can be studied using SPR (62). To study the dissociation of the wild type and mutant ERCC1-XPF complexes directly, they were immobilized via the C-terminal histidine tag of ERCC1 on Ni^{2+}-NTA chips. The increase in SPR response upon loading the ERCC1-XPF complex shows that the complex can be successfully loaded within 50 s (Fig. 1*F*). Upon buffer elution, a drop of the SPR response is observed until it reaches a plateau at about 50% of the initial response. In theory, the SPR decay could be due to a 50% loss of the ERCC1-XPF complex from the NTA chip. Alternatively, given the similar molecular weights of XPF and ERCC1, this reduction can also be explained by the dissociation of XPF from ERCC1, where His-tagged ERCC1 remains bound to the Ni^{2+}-NTA chip. Because the F231L mutation will affect this SPR decay, as we will see below, dissociation is the more likely interpretation. Upon continued elution for 1000 s, we observe the return of the SPR response to its starting level due to dissociation of His-tagged ERCC1 from the Ni^{2+}-NTA chip (not shown).

The dissociation of wild type and mutant ERCC1-XPF was followed by SPR at different heterodimer concentrations, temperatures, and salt concentrations (*cf.* Fig. 1*F*), as described in more detail under "Experimental Procedures." Negative response at temperatures above 25 °C suggests that the SPR results are biased by ERCC1 precipitation. Data could be reliably fitted with single exponential decays, although it was evident that also slower processes contributed to the SPR response. In multiple SPR responses, a second decay with k_{off}^{app} of $\sim 3 \times 10^{-3}$ s^{-1} was identified, corresponding to the slow release of His-tagged ERCC1 monomer and ERCC1-XPF from the chip. At 25 °C and lower temperatures, at lower ionic strength, the dissociation rates k_{off}^{app} for wild type and mutant seem only marginally different (Table 1). For example, at 12 °C and low ionic strength, the k_{off}^{app} for the F231L mutant was 1.9 ±

Downloaded from http://www.jbc.org/ at Universiteitsbibliotheek Utrecht on December 3, 2015

0.3×10^{-2} s^{-1}, whereas for wild type ERCC1-XPF, k_{off}^{app} was $1.3 \pm 0.2 \times 10^{-2}$ s^{-1}. At higher ionic strength, the k_{off}^{app} for the wild type ERCC1-XPF is similar to the k_{off}^{app} at 50 mM NaCl, with a value of $1.43 \pm 0.03 \times 10^{-2}$ s^{-1}, whereas for the F231L mutant, the dissociation rate k_{off}^{app} significantly increases to $3.0 \pm 0.3 \times 10^{-2}$ s^{-1}.

NMR Spectral Differences between Wild Type and F231L ERCC1-XPF—NMR assignments for the F231L mutant ERCC1-XPF $(HhH)_2$ complex were obtained using standard triple resonance techniques and analysis of three-dimensional NOESY spectra, whereas those for the wild type complex were already available (18). The two-dimensional ^{1}H,^{15}N HSQC spectra of the wild type and F231L mutant ERCC1-XPF $(HhH)_2$ complexes are similar but do show differences, both in chemical shift and in intensity (Figs. 2 and 3). Comparing the chemical shifts (Fig. 3, *A* and *C*) it is noted that differences are mostly close to the F231L mutation site (*i.e.* for ERCC1 helix α Leu^{227}, Gln^{229}, Asp^{230}, Val^{232}, Ser^{233}, and Val^{235}), but significant chemical shift differences are also found for residues farther away, both in the ERCC1 and XPF $(HhH)_2$ domains. Among these distant residues are Met^{224}, Glu^{237}, Thr^{252}–Leu^{260}, Leu^{263}, Arg^{268}, and Gly^{278} in ERCC1 helices α and γ and Phe^{894}–Ser^{899} in the XPF C-terminal helix. Whereas the local chemical shift differences could be merely the effect of the different chemical nature of Phe^{231} and Leu^{231}, the distant differences may reflect structural differences, which could influence the association and dissociation behavior of the ERCC1-XPF complex. Fig. 3*C* shows that the observed chemical shift differences are most pronounced for residues that locate in the wild type structure at the ERCC1-XPF interface, suggesting that the monomeric folds of ERCC1 and XPF are very similar

TABLE 1
Dissociation rates for wild type and F231L mutant ERCC1-XPF $(HhH)_2$ heterodimers measured by SPR

ERCC1-XPF	k_{off}^{app} 12 °C	k_{off}^{app} 20 °C	k_{off}^{app} 25 °C
		10^{-2} s^{-1}	
50 mM NaCl			
Wild type	1.3 ± 0.2	1.5 ± 0.1	2.3 ± 0.3
F231L	1.9 ± 0.3	2.0 ± 0.5	3.0 ± 0.1
150 mM NaCl			
Wild type	1.43 ± 0.03		
F231L	3.0 ± 0.3		

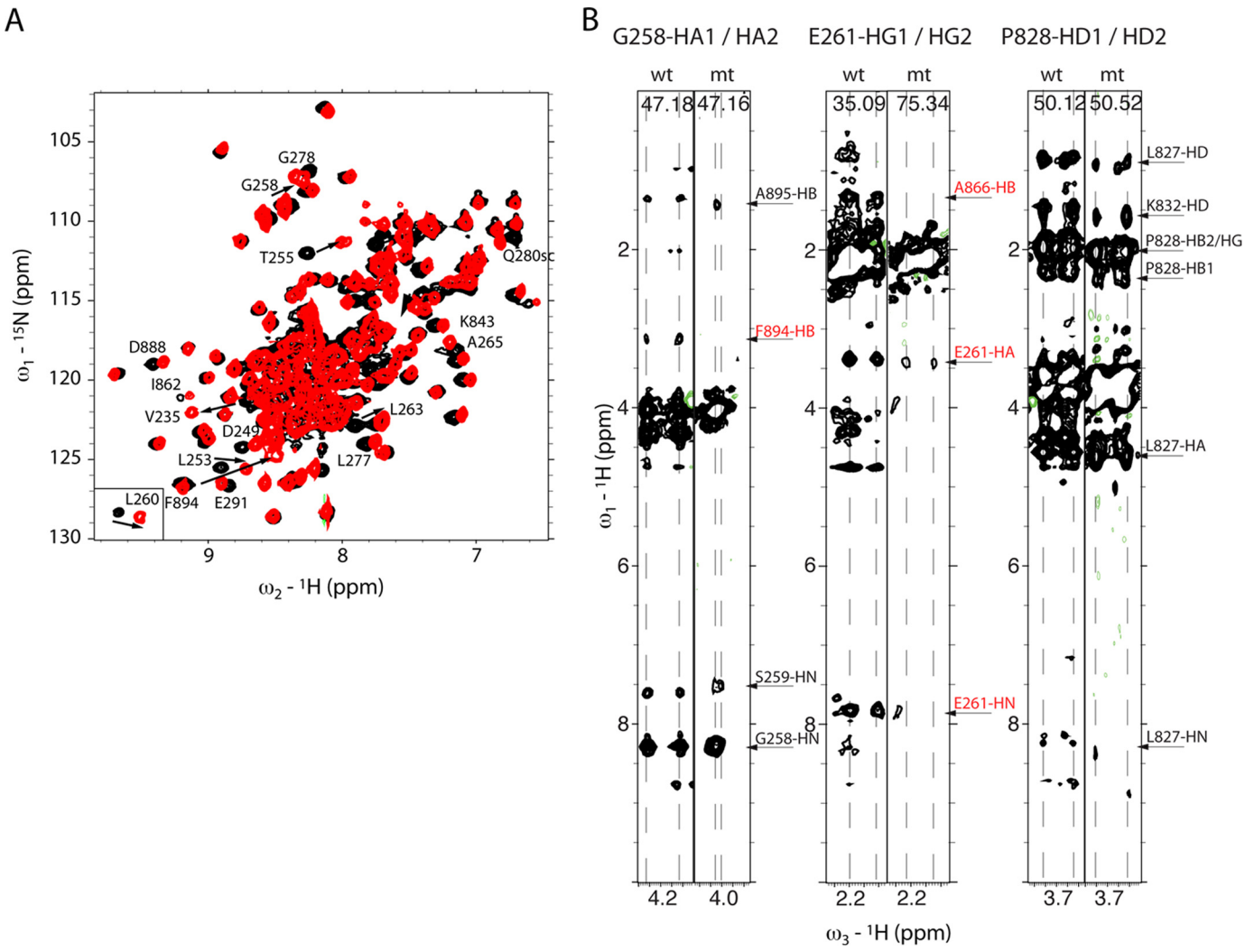

FIGURE 2. **Comparison of NMR spectra for wild type and F231L ERCC1-XPF $(HhH)_2$ heterodimers.** *A*, overlay of ^{1}H,^{15}N HSQC for wild type (*black*) and F231L mutant (*red*) ERCC1-XPF $(HhH)_2$ heterodimer. *B*, selected regions from a three-dimensional NOESY-^{1}H,^{13}C HSQC spectrum comparing the wild type and F231L ERCC1-XPF $(HhH)_2$ heterodimers.

Downloaded from http://www.jbc.org/ at Universiteitsbibliotheek Utrecht on December 3, 2015

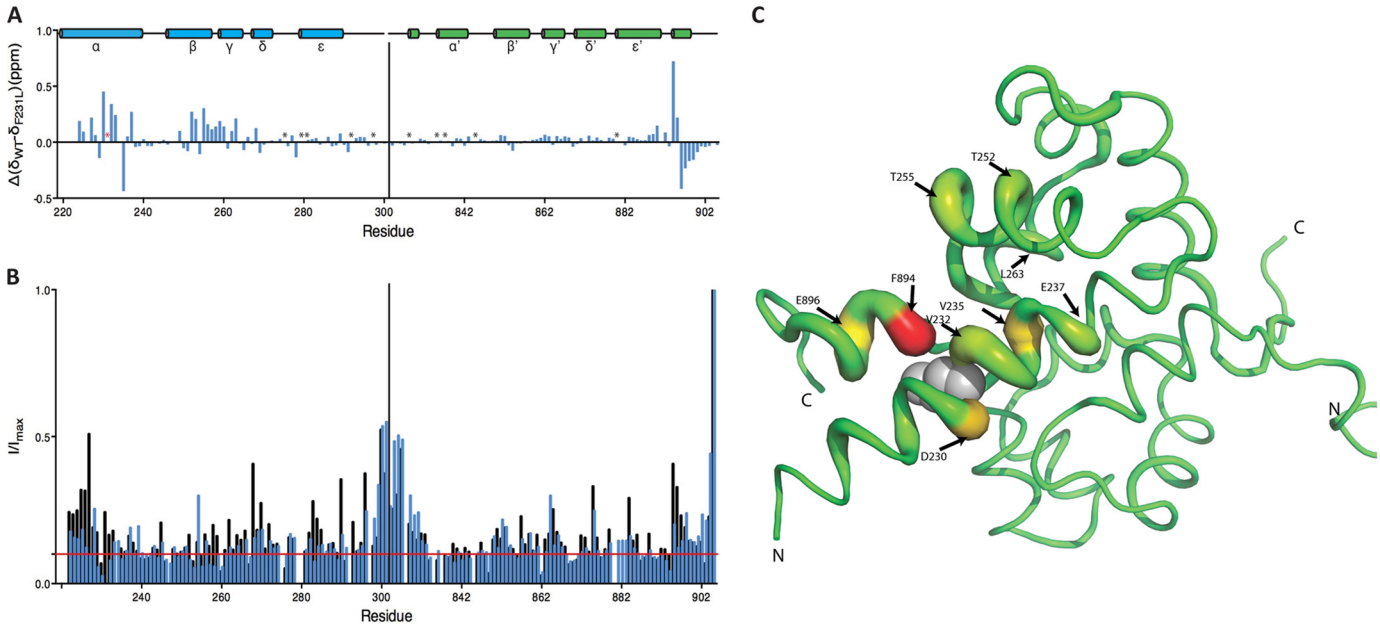

FIGURE 3. **$^{1}H,^{15}N$ HSQC chemical shift and signal intensity analysis of wild type and F231L ERCC1-XPF $(HhH)_2$ heterodimers.** *A*, chemical shift differences for amide protons: $\Delta H^N(\delta_{WT}-\delta_{F231L})$ (in ppm). Unassigned residues are marked with an *asterisk*, *red* for the mutation site. *B*, variation in $^{1}H,^{15}N$ HSQC cross-peak intensities. The intensities are depicted in *black* for the wild type and in *blue* for the F231L mutant. Values are normalized to the highest signal intensity (Lys^{905}). The *red horizontal line* is the average of the signal intensity for residues in secondary structure elements of the wild type ERCC1-XPF $(HhH)_2$ heterodimer. *C*, projection of chemical shift differences on the structure of the wild type ERCC1-XPF $(HhH)_2$ heterodimer, representing residues with maximum perturbation as *red broad ribbons*, residues with medium perturbation as *yellow broad ribbons*, and residues with small to no difference in *green*. The F231L mutation site is represented as *gray spheres*.

in both complexes and that the mutation mainly affects contacts between ERCC1 and XPF.

Intensity differences between the two-dimensional $^{1}H,^{15}N$ HSQC spectra of wild type and F231L mutant ERCC1-XPF were noted as well (Fig. 3*B*). The graph shows a plateau that coincides with regions that in the wild type ERCC1-XPF $(HhH)_2$ complex have stable secondary structure. F231L ERCC1-XPF shows reduced intensity for residues that are directly contacting the mutation site in the wild type structure (*i.e.* for residues in helices α, β, and γ of ERCC1 (Gln^{229}, Asp^{230}, Val^{232}, Ser^{233}, Thr^{252}, Leu^{253}, Thr^{255}, Phe^{257}, Gly^{258}, and Ser^{259}) and for residues in the C-terminal helix of XPF (Thr^{892}, Ser^{893}, and Phe^{894})). In fact, lack of signal intensity might be the reason that the amide proton of Leu^{231} could not be unambiguously assigned. The differences between the wild type and F231L ERCC1-XPF HSQC signal intensity probably reflect increased local dynamics in F231L ERCC1-XPF at the mutation site.

Amide Proton Exchange—The interface of the complex of the $(HhH)_2$ domains of wild type ERCC1-XPF is formed by hydrophobic interactions involving several aromatic phenylalanine residues (of which two important ones are the pseudosymmetric anchors Phe^{293} (in ERCC1) and Phe^{894} (in XPF)) and several intermolecular hydrogen bonds (Ser^{259} HG···O Thr^{892}, Glu^{261} HN···O Ile^{890}, Phe^{293} HN···O Lys^{860}, Asn^{834} HN···O Phe^{293}, Asn^{834} HD21···O Pro^{292}, His^{891} HD1···OE2 Glu^{261}, and Ala^{895} HN···O Gly^{258}) (18, 21). The importance of hydrogen bonding for the stability of the ERCC1-XPF complex and the effect of the F231L mutation on this stability were studied by amide proton/deuterium (H/D) exchange, similar as before for homodimeric XPF $(HhH)_2$ (38). For this, we acquired a series of two-dimensional $^{1}H,^{15}N$ HSQC spectra of wild type and mutant ERCC1-XPF $(HhH)_2$ heterodimer freshly dissolved in $^{2}H_2O$ (Fig. 4) and compared the H/D exchange for all residues that were still visible after the dead time of the experiment (*i.e.* 8 min) and were non-overlapping in the spectra of the wild type ERCC1-XPF heterodimer as well as the mutant F231L. A comparison of the H/D exchange could be made for residues Cys^{238}, Thr^{240}–Val^{242}, Leu^{253}, Thr^{255}, Ser^{259}–Glu^{261}, Leu^{263}, Ala^{265}, Ser^{267}, Leu^{271}, Ala^{272}, Ala^{282}, Leu^{285}, His^{290}, and Leu^{294} of ERCC1 and the residues Asp^{839}, Leu^{842}, Lys^{847}, Met^{856}, Val^{859}, Asn^{861}–Ala^{863}, Leu^{873}, Thr^{874}, Ile^{876}, Leu^{877}, Ala^{883}, and Gln^{885}–Thr^{892} of XPF. Overall, we note similar H/D exchange rates for wild type and mutant ERCC1-XPF $(HhH)_2$ heterodimer, with slow exchanging amide protons in the core of the complex and quick exchange for residues that are more surface-exposed. Only the ERCC1 residue Leu^{253} of the F231L mutant shows significantly faster exchange than in the wild type, which suggests an increased solvent accessibility for helix β of ERCC1 (Fig. 4*C*).

Whereas H/D exchange measures slow (minutes to hours) amide proton exchange (63), CLEANEX-PM experiments can probe fast (subsecond) solvent exchange (49). Also with CLEANEX-PM, no significant exchange differences were observed between the wild type and mutant ERCC1-XPF (data not shown). The only exception for which solvent exchange was reduced in the mutant is the amide proton of Val^{235} in helix α of ERCC1, which is four residues apart from the F231L mutation site and hydrogen-bonded to residue 231 in the wild type structure. If anything, this suggests even a slightly increased stability of helix α in F231L ERCC1 as compared with the wild type system.

Downloaded from http://www.jbc.org/ at Universiteitsbibliotheek Utrecht on December 3, 2015

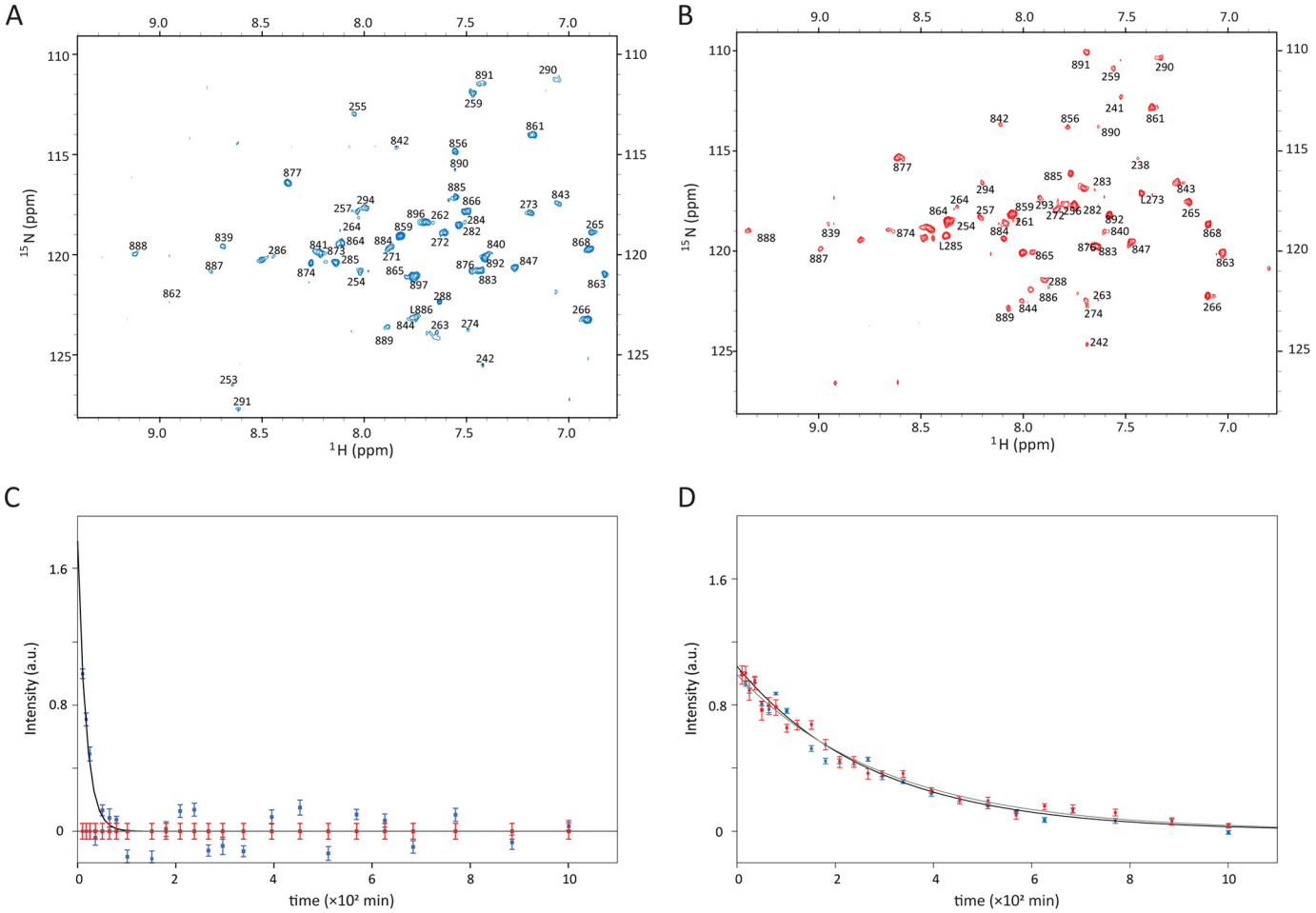

FIGURE 4. **Proton-deuterium exchange of wild type and F231L ERCC1-XPF $(HhH)_2$ heterodimers.** Shown are initial ^{1}H,^{15}N HSQCs after the dead time of the experiment for wild type (*A*) and mutant (*B*) ERCC1-XPF heterodimers. Shown is the time course of the H/D exchange behavior of Leu^{253} (*C*) and Val^{859} (*D*). Signal intensities for the wild type system are shown in *blue*, and signal intensities for the mutant are shown in *red*.

In summary, between the wild type and mutant ERCC1-XPF $(HhH)_2$ heterodimers, differences in amide proton chemical shifts and in NMR intensities are seen for regions in direct contact with the mutation site and for residues localized near the Phe^{894} anchor of the interface of ERCC1-XPF. The solvent exchange experiments indicate that the integrity of the ERCC1 and XPF monomers is hardly affected by the F231L mutation. In line with the thermal stability analysis, this also indicates that the reduced stability of ERCC1-XPF that we observed is not caused by differences in secondary structure stability but is rather the result of different association or dissociation properties of the $(HhH)_2$ complex.

Temperature-dependent Chemical Shift Changes—Temperature-dependent chemical shift changes for protein amide protons in hydrogen bonds are usually linear as a function of temperature, and the $\Delta\delta/\Delta T$ gradients can be related to hydrogen bond strengths (45, 46). Slow amide proton exchange combined with a temperature coefficient more positive than −4.5 ppb/K indicates the presence of a hydrogen bond, whereas fast exchange combined with a temperature coefficient more negative than −4.5 ppb/K indicates the absence of a hydrogen bond. The residues with significant differences between wild type and mutant ERCC1-XPF (*cf.* Table 2) are mostly located in the direct vicinity of the mutation site or around the nearby anchor Phe^{894}, indicating that the mutation causes mainly a local structural effect. However, overall, with only a few exceptions, the temperature coefficients are more negative for the F231L mutant than wild type ERCC1-XPF, suggesting a reduced overall hydrogen bond stability of F231L ERCC1-XPF.

TABLE 2

Residues with significantly different proton temperature coefficients ($\Delta\delta/\Delta T$) for wild type and F231L mutant ERCC1-XPF $(HhH)_2$ heterodimers measured by NMR

	$\Delta\delta/\Delta T$	
	Wild type	F231L mutant
	ppb/K	
Val^{235}	−2.932	−9.358
Cys^{238}	2.733	1.095
Leu^{239}	−2.684	−5.859
Leu^{242}	−2.932	−4.450
Gln^{251}	−6.294	−2.527
Leu^{253}	−4.080	−2.476
Thr^{255}	−4.972	−0.051
Ser^{259}	−5.494	1.977
Leu^{263}	−3.992	−2.01
Ala^{265}	−0.062	−2.125
Ile^{890}	−1.831	−1.350
Phe^{894}	−2.565	2.415

NMR Structure—To see whether the increased dissociation of the F231L mutant ERCC1-XPF complex is caused by struc-

Downloaded from http://www.jbc.org/ at Universiteitsbibliotheek Utrecht on December 3, 2015

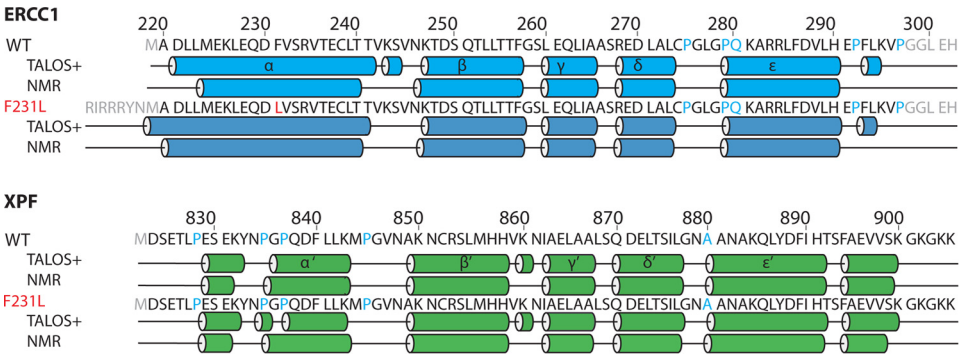

FIGURE 5. **Secondary structure elements of wild type and F231L ERCC1-XPF $(HhH)_2$ heterodimers.** Shown are chemical shift-derived secondary structure elements for wild type (WT) and mutant (F231L) ERCC1 predicted by TALOS+ and secondary structure elements detected in the lowest energy structure after (re)calculation of the NMR ensembles. *Top*, ERCC1; *bottom*, XPF. Unassigned amide protons are shown in *blue* in the sequence. The N-terminal extension assigned in mutant ERCC1, the His_6 tag, and N-terminal methionines of the construct are shown in *gray*.

tural differences between the wild type and mutant, we set out to determine the NMR structure of the F231L ERCC1-XPF $(HhH)_2$ heterodimer and to compare it with existing structures of wild type ERCC1-XPF. To allow direct comparison, we recalculated the earlier reported wild type ERCC1-XPF $(HhH)_2$ heterodimer NMR structure with exactly the same parameters as the F231L mutant.

The dispersion and cross-peak positions of the two-dimensional ^1H,^{15}N HSQC spectra of the $(HhH)_2$ complexes of wild type and F231L ERCC1-XPF are rather similar, demonstrating that the wild type and F231L mutant complexes are both well folded and structurally not very different (Fig. 2). Of 180 residues of F231L ERCC1-XPF, the amide protons of 161 residues could be assigned. No assignments could be made for five residues of the ERCC1 C-terminal His_6 tag and a few N-terminal residues of both ERCC1 and XPF $(HhH)_2$ domains. This leaves only three other residues for which no amide resonances could be assigned, namely Leu^{231}, Gln^{280}, and Ala^{880}. For the point mutation Leu^{231}, it should be noted that although its amide nitrogen resonance was not found, most other atoms of Leu^{231} could be assigned.

As pointed out above, the differences in chemical shifts between wild type and mutant $(HhH)_2$ complexes are relatively small and mainly localized around the mutation site. Based on the chemical shift values for both proteins, the overall arrangement of the α-helices is not altered by the mutation, and in the wild type as well as the mutant complex, residue 231 is present in an α-helix (Fig. 5). The N-terminal helix (α) in wild type ERCC1, appears shortened, but this may be due to lack of data because the crystal structure shows that the segment Ala^{220}–Thr^{240} is also α-helical in wild type ERCC1-XPF (21). For the F231L mutant ERCC1-XPF studied here, helix α spans from residue Asp^{221} to Thr^{240}.

The NMR structures of the wild type and F231L ERCC1-XPF $(HhH)_2$ heterodimeric complexes were determined using NOE-based distance restraints and chemical shift-based torsion angle restraints (Fig. 6*A* and Table 3). The total number of NOEs used to calculate the structure of the F231L mutant ERCC1-XPF is lower than that for wild type. Still, the overall quality of the wild type and F231L mutant ERCC1-XPF structures is similar. The secondary structure elements in the wild type and mutant structure ensembles are very similar. The helices α–ϵ of wild type ERCC1 (*i.e.* Met^{224}–Thr^{240}, Lys^{247}–Phe^{257}, Leu^{260}–Ala^{265}, Arg^{268}–Ala^{272}, and Pro^{279}–His^{290}, respectively) and the helices α'–ϵ' of XPF (*i.e.* Glu^{829}–Glu^{831}, Pro^{837}–Lys^{843}, Ala^{849}–His^{858}, Ile^{862}–Ala^{866}, Gln^{870}–Leu^{877}, Ala^{880}–His^{891}, and Phe^{894}–Lys^{900}, respectively) are almost invariably present in all conformers of the ensemble of mutant ERCC1-XPF. However, some differences are evident from the NMR structures. For the wild type heterodimer, assignments are lacking for the N terminus of ERCC1, which obviously leads to a lower number of NOEs for this part of the protein. Therefore, as pointed out above, helix α of wild type ERCC1 starts at Met^{224}, whereas that of F231L ERCC1 starts at Asp^{221} (Fig. 6*A*).

Although the two NMR ensembles of wild type and mutant ERCC1-XPF are well defined and the overall fold is the same, the structures show small local differences. The closest-to-mean root mean square deviation values for all heavy atoms are 1.35 Å for ERCC1 residues 227–294, 1.15 Å for the XPF core residues 831–896, and 1.29 Å for both regions together. This indicates small but genuine differences between the two structures and that the XPF part is more similar than the ERCC1 monomer.

After superimposing the backbones, interesting NOE-based differences are seen for the side chain orientations of the two complexes. For example, Fig. 2*B* shows selected NOE patterns for residues Gly^{258}, Glu^{261}, and Pro^{828} comparing wild type and F231L ERCC1-XPF. The NOE intensities for residues Gly^{258} and Glu^{261} are clearly different for both complexes, consistent with local structural differences near the mutation point, whereas farther away from the mutation site (*e.g.* residue Pro^{828}), no structural effects occur. In wild type ERCC1-XPF, Phe^{231} is embedded deeply in the core of the $(HhH)_2$ heterodimer structure (Fig. 6*A*). Its aromatic side chain and the backbone show short distances (<4 Å) to ERCC1 residues Leu^{227}–Val^{235} of the same helix, but the residue is also close to Ser^{259} and Leu^{260} of ERCC1 and to residues Phe^{889}, Ile^{890}, Thr^{892}, Ser^{893}, and Phe^{894} of XPF. The aromatic side chain of Phe^{231} in wild type ERCC1-XPF is packed between the aromatic rings of Phe^{894} and Phe^{889}, making a T-shaped arrangement with respect to them. The F231L mutation does not influence the integrity of helix α, despite a very different side chain orientation of residue Leu^{231} as compared with Phe^{231} in wild type (Figs. 6 (*A*–*C*) and 7). In the mutant, Leu^{231} maintains similar distances and angles toward residues Leu^{227}–Val^{235} of ERCC1 and residues Phe^{889} and Ser^{893} of XPF. However, the mutation allows

Downloaded from http://www.jbc.org/ at Universiteitsbibliotheek Utrecht on December 3, 2015

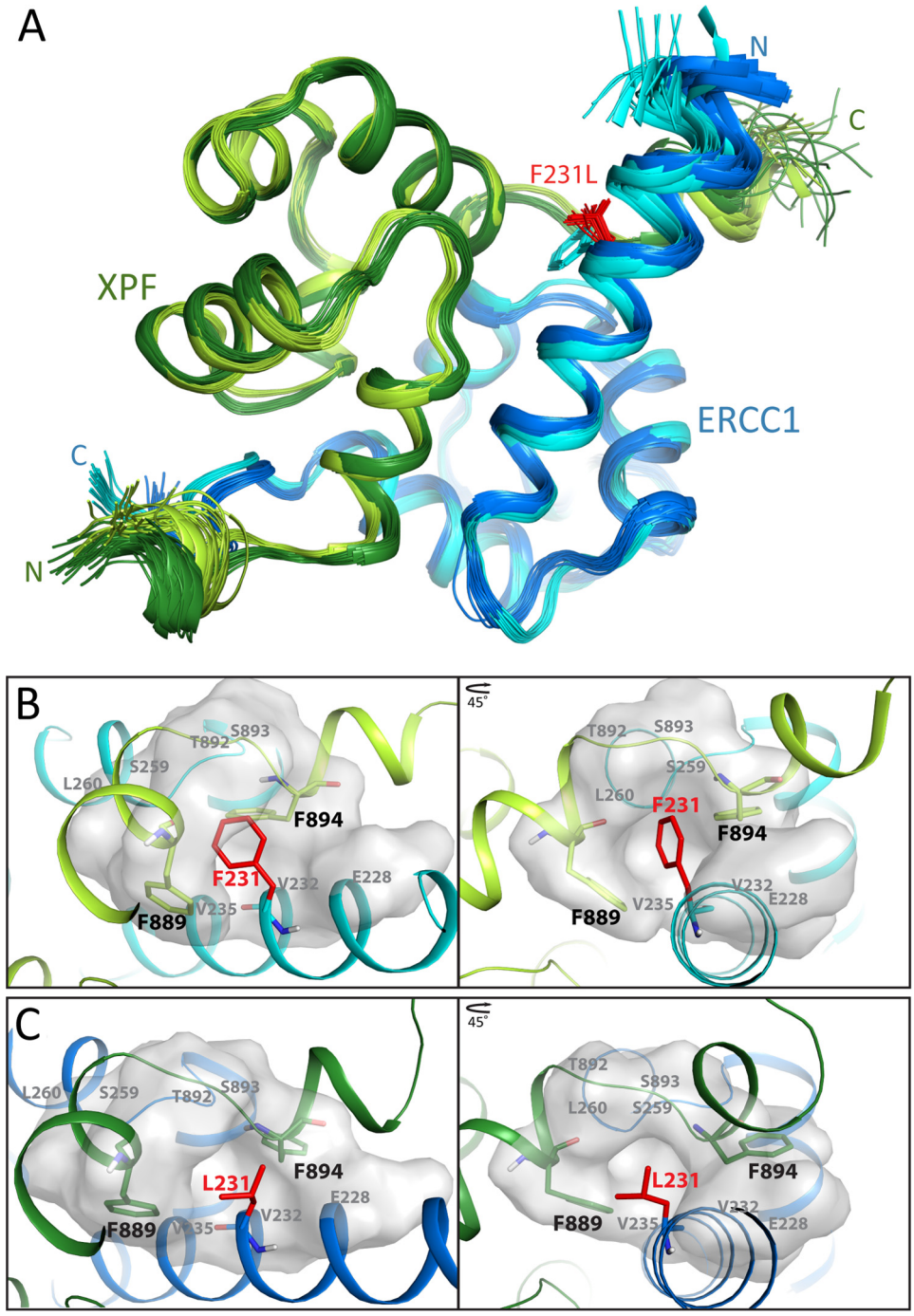

FIGURE 6. **Solution structures of wild type and F231L ERCC1-XPF $(HhH)_2$ heterodimers.** *A*, superimposed NMR ensembles of F231L and recalculated wild type ERCC1-XPF $(HhH)_2$. The backbone of ERCC1 is *colored blue* (*cyan*, wild type; *blue*, mutant); the backbone of XPF is colored *green* (*lemon yellow*, wild type; *dark green*, mutant). The mutated residue Leu^{231} is shown in *red*. Shown are a surface depiction and side chain organization for phenylalanines Phe^{231}, Phe^{889}, and Phe^{894} of wild type ERCC1-XPF $(HhH)_2$ (*B*) and for residues Leu^{231}, Phe^{889}, and Phe^{894} of F231L ERCC1-XPF $(HhH)_2$ (*C*). Backbones, Phe^{889}, and Phe^{894} are *colored* as in *A*; the side chain of Phe^{231}/Leu^{231} is *colored* in *red*, and the labels in *gray* depict residues surrounding Phe^{231}/Leu^{231}.

the side chain of Phe^{894} to reorient. Consequently, at the ERCC1 region flanking the XPF C terminus, contacts are lost between residues Phe^{894}, Gly^{258}, Ser^{259}, and Leu^{260}, and the interactions between the segments Ile^{890}–His^{891} and Leu^{260}–Glu^{261} are weakened. The reduction in aromatic ring interactions probably explains part of the differences in chemical shifts for segments Leu^{227}–Glu^{237} and Asp^{252}–Leu^{263} of ERCC1 and the segment Thr^{892}–Ser^{899} of XPF (Fig. 3).

Due to the F231L mutation, the aromatic side chains of Phe^{889} and Phe^{894} cannot maintain their T-shaped arrangement with respect to residue 231 (Fig. 6, *B* and *C*). In the wild type complex, Phe^{889} contacts residues Asp^{230}, Phe^{231}, Arg^{234}, Val^{235}, Cys^{238}, and Leu^{260} of ERCC1 and Met^{844}, Pro^{845}, the N-terminally located helix ϵ' (Gln^{885}–Asp^{888}), and segment Ile^{890}–Thr^{892} of XPF. In the mutant, Phe^{889} modestly changes its contacts with Leu^{260} of ERCC1, whereas most interactions

Downloaded from http://www.jbc.org/ at Universiteitsbibliotheek Utrecht on December 3, 2015

TABLE 3
Statistics of the structure calculations for wild type and mutant ERCC1-XPF $(HhH)_2$ heterodimer

	Wild type	F231L mutant
Root mean square deviation (Å)[a]		
ERCC1 (backbone/heavy atom)	0.21/0.53	0.24/0.71
XPF (backbone/heavy atom)	0.22/0.49	0.30/0.68
Complex (backbone/heavy atom)	0.24/0.53	0.30/0.72
No. of peaks		
Assigned	11,077	8686
Total	12,947	11,365
No. of experimental restraints		
Intra	895	561
Sequential	1218	738
Medium	1246	599
Long intra	777	303
Long inter	478	223
Total NOE	4614	2424
Dihedrals	197	267
Hydrogen bonds	56	63
Consistent violations		
NOE > 0.5	0	0
Dihedral > 5	0	1 (F889 ϕ[b])
WhatCheck[a,c]		
Ramachandran plot appearance	−2.044 ± 0.209	−2.703 ± 0.171
Second generation packing quality	4.312 ± 1.403	3.156 ± 1.304
$\chi1 - \chi2$ rotamer normality	−4.879 ± 0.167	−5.085 ± 0.322
Backbone conformation	−0.412 ± 0.279	−4.954 ± 0.209
Ramachandran plot[a,c]		
Favorable	94.4	96.8
Additionally allowed	5.6	3.2
Generously	0.0	0.0
Disallowed	0.0	0.0

[a] Core residues 227–294 (ERCC1) and 831–896 (XPF).
[b] The violation is introduced by the water refinement.
[c] Results from iCING.

within XPF remain. The situation for the Phe^{894} anchor, however, is very different. Whereas most contacts with the neighboring residues in the XPF Phe^{894} interaction pocket (Thr^{892}–Ser^{899}) are still present in the mutant, the intermolecular contacts with ERCC1 are strongly altered due to side chain reorientations for residues Gln^{229}, Leu^{231}, and Val^{235} of helix α, residues Leu^{254} and Phe^{257} of helix β, and residues Glu^{261} and Leu^{263} of helix γ. It was found that in addition to these differences in phenylalanine contacts, several other residues of the complex show side chain reorientations. Most of these residues (Glu^{269}, Leu^{273}, Asn^{280}, Arg^{284}, Tyr^{833}, and Cys^{852}) are at the surface of the complex (Fig. 7), and the observed differences can be due to lack of NOEs. However, for the interface residues Lys^{843}, Ile^{862}, Leu^{865}, and Tyr^{887}, the story is different; whereas the backbones of the twenty structures are very well superimposed, the differences between the wild type and mutant consistently show considerable changes in side chain orientation (Fig. 7). Finally, the F231L mutation leads to not only a significant reduction in the intermolecular hydrophobic packing involving the Phe^{894} anchor but also a slight increase (0.3 ± 0.01 Å) of the distance between the backbone amide of XPF Phe^{894} and the backbone carboxyl of ERCC1 Gly^{258}, causing the hydrogen bond between the backbone amide of Ala^{895} and the backbone carboxyl of Gly^{258} to vanish completely. In addition, as a consequence of the reorientation of Glu^{261}, the imidazolium-carboxyl hydrogen bond between His^{891} and Glu^{261} disappears. Also, the interactions between Ile^{264} and XPF residue Ala^{863}, between Leu^{289} and Phe^{840}, and between the side chain of Lys^{843} and ERCC1 residues Glu^{237}, Cys^{238}, and Thr^{241} of ERCC1 appear diminished. Overall, the small structural changes initiated by the F231L mutation lead to local, modest conformational effects in the direct vicinity of the mutation, which accumulate in a number of differences affecting the interface between ERCC1 and XPF.

Discussion

At the moment, the most severe cases of ERCC1-XPF deficiency are described for two patients with a F231L mutation in ERCC1 (28, 31). Genetic and functional studies have revealed that one patient carries a null allele and a F231L allele, and the other patient carries a biallelic F231L mutation. This F231L ERCC1 mutant in complex with XPF retains enzymatic activity. Analogous to patients with XPF mutations, this phenotype is a consequence of low levels of ERCC1-XPF (28, 31). Earlier structural studies of the wild type ERCC1-XPF complex have shown that the interface of ERCC1-XPF is composed of two pseudo-symmetric hydrophobic cavities tightly embracing anchor residues and a third, large hydrophobic contact region (Fig. 8) (18, 21). The first anchor is formed by the aromatic ring of ERCC1 Phe^{293}, which fills the cavity composed of residues Leu^{294} of ERCC1 and Tyr^{833}, Asn^{834}, Pro^{837}, Gln^{838}, Leu^{841}, Met^{856}, Asn^{861}, and Ile^{862} (helices α' and β') of XPF. The second anchor is formed by the XPF residue Phe^{894} aromatic ring, which fits into the cavity comprising ERCC1 residues Phe^{231}, Val^{232}, Val^{235}, Leu^{254}, Gly^{258}, and Ser^{259} (helices α and β) and XPF residues Phe^{889}, Thr^{892}, Ser^{893}, and Ala^{895}. The interactions in both anchor regions are stabilized by multiple intermolecular and intramolecular hydrogen bonds. The third contact region lies in between both anchor regions and involves the pseudo-symmetrically positioned ERCC1 helices α and γ and XPF helices α', γ', and ϵ'. In this region, the aromatic side chain of Phe^{840} plays a major role for intermonomer contacts. ERCC1 residues Cys^{238}, Leu^{239}, Thr^{241}, Leu^{260}, Leu^{263}, Ile^{264}, Leu^{285}, Val^{288}, and Leu^{289} surround Phe^{840}, and their contacts with residues Gly^{836}, Pro^{837}, Gln^{838}, Asp^{839}, Leu^{841}, Leu^{842}, Lys^{843}, Met^{844}, and Ile^{862} in the pseudosymmetrically positioned region of XPF support this interaction. Furthermore, the short γ, ϵ, γ', and ϵ' helices show contacts between the side chains of Ile^{264} and Leu^{289} in ERCC1 and Ala^{863} and Ala^{866} in XPF and between Leu^{260} in ERCC1 and Phe^{889} in XPF. In addition, the backbone carbonyl of Lys^{843} contacts the side chain guanidinium group of Arg^{234}, whereas the NH_3^+ group of the Lys^{843} side chain contacts the side chain carboxyl of Glu^{237} (Fig. 7).

In wild type ERCC1, Phe^{231} is located in helix α. It is part of the cavity containing anchor Phe^{894} and completely embedded in the heterodimer core. The side chain of Phe^{231} is located between the aromatic rings of Phe^{894} and Phe^{889} with stabilizing T-shaped arrangements (64). In the F231L mutant, the aromatic side chain of Phe^{889} maintains its orientation, whereas residues Leu^{231} and Phe^{894} reorient their side chains toward the surface of the protein (Fig. 8*B*). This means not only that the interactions of the benzyl group of Phe^{231} are missing in the Phe^{894} hydrophobic cavity but also that the benzyl group of Phe^{894} can no longer function as an anchor stabilizing the complex. In addition, the side chain of Phe^{894} becomes exposed, and a smaller hydrophobic interaction surface is present in the mutant (especially concerning residues in helix β). This and the

Downloaded from http://www.jbc.org/ at Universiteitsbibliotheek Utrecht on December 3, 2015

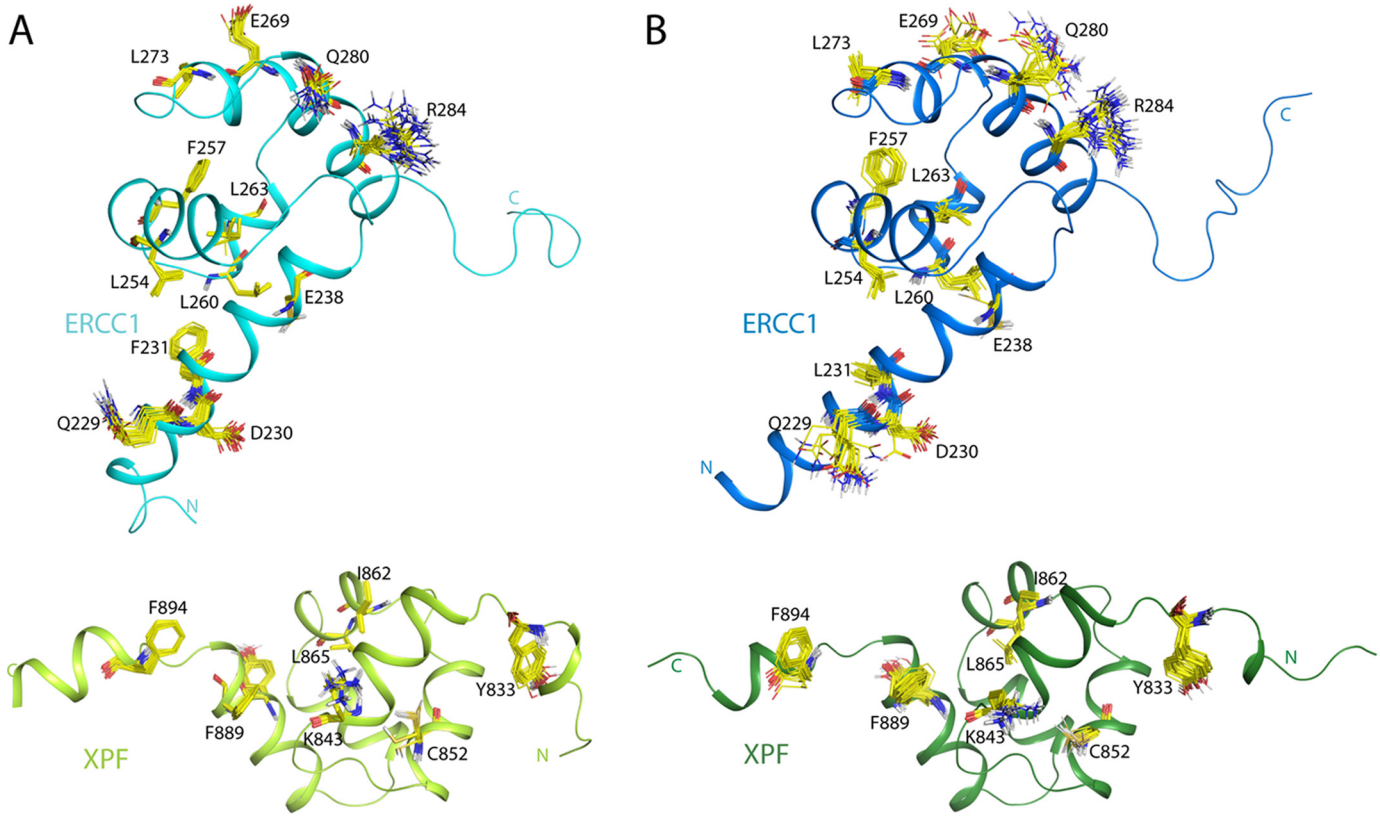

FIGURE 7. **Side chain orientations in wild type and F231L ERCC1-XPF $(HhH)_2$ heterodimer.** Side chains of residues showing the largest differences between the NMR ensembles are depicted for the recalculated complex of wild type ERCC1 $(HhH)_2$ (*top*) and XPF (*bottom*) (*A*) and the calculated complex of F231L mutant ERCC1 $(HhH)_2$ (*top*) and XPF (*bottom*) (*B*). Backbone *coloring* is as in Fig. 6*A*. Amino acid side chains are shown in *yellow*, with polar hydrogen in *gray*, oxygen in *red*, and nitrogen in *blue*. The monomers of ERCC1 and XPF are separated for a better view.

lack of aromatic ring interactions destabilize ERCC1-XPF by increasing the dissociation rate of the complex.

The reduced hydrophobic character for the interactions within the F231L ERCC1-XPF complex interface implies that the electrostatic contributions to the interactions should relatively increase. Indeed, when increasing the ionic strength, the dissociation rate for wild type ERCC1-XPF did not change much (*cf.* Table 1), whereas it increased for mutant ERCC1-XPF. The higher dissociation rate for the mutant indicates that the interactions at the interface of mutant ERCC1-XPF are more electrostatic in nature than that of wild type ERCC1-XPF (65, 66).

A comparison of wild type and mutant ERCC1-XPF $(HhH)_2$ complexes shows that the majority of structural differences is limited to regions in direct proximity of Leu^{231}. These include the α and γ helices of ERCC1 and the C-terminal helix of XPF. The amides surrounding Leu^{231} also show a significant decrease in $^{1}H,^{15}N$ HSQC signal intensity as compared with those surrounding Phe^{231} in the wild type, and the signal of the amide of Leu^{231} was even completely lacking. This loss of signal intensity can be explained by the occurrence of slow internal dynamics caused by millisecond motional effects of the Phe^{894} aromatic ring. The observed structural differences, mainly at the interface, could lead to instability of the ERCC1-XPF complex. Our stability analysis of the ERCC1-XPF $(HhH)_2$ domains using far-UV CD spectroscopy and ThermoFluor analysis shows that the lower temperature stability of the F231L ERCC1-XPF complex is not due to a reduced intrinsic ERCC1 and XPF stability but rather to a faster dissociation of the heterodimer. Indeed, using SPR, we could directly demonstrate that this dissociation is significantly faster for the mutant than for the wild type complex.

In conclusion, the replacement of Phe^{231} by leucine appears to have only a small effect on the ERCC1 and XPF monomer structures and *in vitro* stabilities and to have no direct functional effect on the DNA binding affinity of ERCC1-XPF at an ss/dsDNA junction. The $(HhH)_2$ heterodimer is still formed, which agrees with the fact that ERCC1-XPF-based DNA repair is still partially functional in patients (28). The mutation influences the hydrophobic interactions between ERCC1 and XPF in the heterodimer, causes faster dissociation of the ERCC1-XPF heterodimer, and in this way reduces the ERCC1-XPF complex stability. With one of the two anchor points disrupted, this increased dissociation of the mutant F231L heterodimer can directly result in a diminished amount of ERCC1-XPF complex. In the cellular context, the separate subunits are unstable because of increased vulnerability to proteolysis. One reason for the intrinsic instability of the individual ERCC1 and XPF molecules might be that uncontrolled DNA binding and endonuclease activities of the separate subunits are a threat to regular DNA metabolism. The lower cellular concentration of the ERCC1-XPF repair complex will reduce the DNA repair capacity and may also lead to the build-up of repair intermediates that wait for the rate-limiting ERCC1-XPF step. This may also disrupt DNA metabolism, leading to enhanced cell death and

Downloaded from http://www.jbc.org/ at Universiteitsbibliotheek Utrecht on December 3, 2015

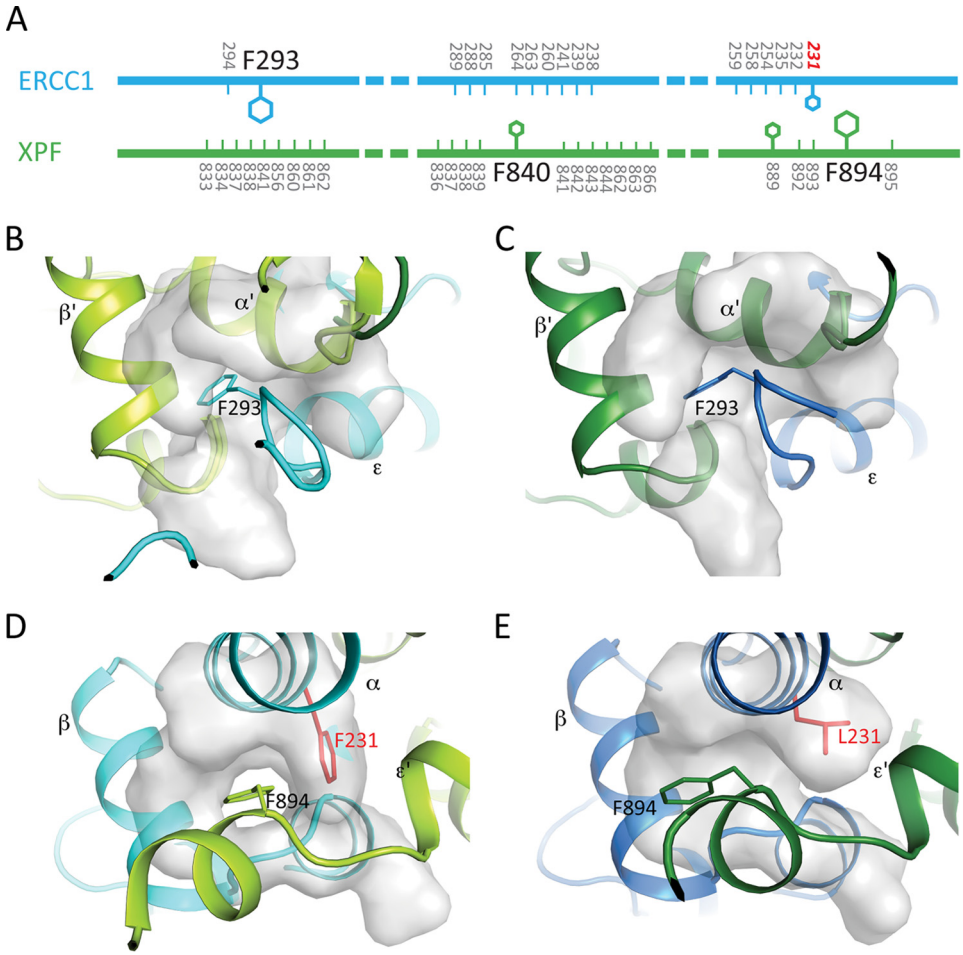

FIGURE 8. **Interaction interface of ERCC1 and XPF and the comparison of Phe^{293} and Phe^{894} cavities at the interface of wild type and F231L mutant ERCC1-XPF.** *A*, schematic representation of the three major interaction regions: anchor Phe^{293}/pocket 1, anchor Phe^{894}/pocket 2, and the hydrophobic core (helices α and γ) surrounding Phe^{840}. ERCC1 is shown in *blue*, and XPF is shown in *green*. Side chains of important phenylalanines are shown. Numbers of residues involved in intermolecular interactions are indicated. Residue 231 is labeled in *red*. The Phe^{293} cavity in the wild type (*B*) and mutant (*C*) ERCC1-XPF $(HhH)_2$ complex is shown. The Phe^{894} cavity in the wild type (*D*) and mutant (*E*) ERCC1-XPF $(HhH)_2$ complex is shown. Side chains of the anchors Phe^{293} and Phe^{894} are shown as *sticks*. The side chain of residue 231 (Phe or Leu) is shown in *red*.

cellular dysfunction, contributing to the premature aging and cancer predisposition of mutants in the ERCC1-XPF complex both in humans and mice. This is most dramatically illustrated by the very severe Cockayne syndrome-like features that are exhibited by the ERCC1-deficient patients.

Author Contributions—M. F., R. B., G. E. F., R. K., J. H. J. H., and N. G. J. J. conceived the study. M. F. purified the mutant ERCC1-XPF complex and was involved in all experiments and analysis. L. K. designed, performed, and analyzed the SPR experiments shown in Fig. 1. M. F. and H. W. performed and analyzed the NMR experiments and determined the NMR structure of the mutant ERCC1-XPF complex. M. F., H. W., G. E. F., and R. B. wrote the paper. All authors reviewed the results and approved the final version of the manuscript.

Acknowledgments—Mark Daniëls and Drs. Hans Ippel, Tobias Madl, Klaartje Houben, Hugo van Ingen, and Konstantinos Tripsianes are gratefully acknowledged for contributions to this work. We also gratefully acknowledge the Infrastructural Centre for Analysis of Molecular Interactions in Ljubljana for use of the SPR facility.

References

1. Hoeijmakers, J. H. J. (2001) Genome maintenance mechanisms for preventing cancer. *Nature* **411,** 366–374
2. Sugasawa, K., Ng, J. M. Y., Masutani, C., Iwai, S., van der Spek, P. J., Eker, A. P. M., Hanaoka, F., Bootsma, D., and Hoeijmakers, J. H. J. (1998) Xeroderma pigmentosum group C protein complex is the initiator of global genome nucleotide excision repair. *Mol. Cell* **2,** 223–232
3. Friedberg, E. C., Walker, G. C., and Siede, W. (1995) *DNA Repair and Mutagenesis*, pp. 135–190, American Society of Microbiology Press, Washington, D. C.
4. Friedberg, E. C., Aguilera, A., Gellert, M., Hanawalt, P. C., Hays, J. B., Lehmann, A. R., Lindahl, T., Lowndes, N., Sarasin, A., and Wood, R. D. (2006) DNA repair: from molecular mechanism to human disease. *DNA Repair* **5,** 986–996
5. Sijbers, A. M., de Laat, W. L., Ariza, R. R., Biggerstaff, M., Wei, Y.-F., Moggs, J. G., Carter, K. C., Shell, B. K., Evans, E., de Jong, M. C., Rademakers, S., de Rooij, J., Jaspers, N. G. J., Hoeijmakers, J. H. J., and Wood, R. D. (1996) Xeroderma pigmentosum group F caused by a defect in a structure-specific DNA repair endonuclease. *Cell* **86,** 811–822
6. Niedernhofer, L. J., Essers, J., Weeda, G., Beverloo, B., de Wit, J., Muijtjens, M., Odijk, H., Hoeijmakers, J. H. J., and Kanaar, R. (2001) The structure-specific endonuclease Ercc1-Xpf is required for targeted gene replacement in embryonic stem cells. *EMBO J.* **20,** 6540–6549
7. Sijbers, A. M., van der Spek, P. J., Odijk, H., van den Berg, J., van Duin, M.,

Downloaded from http://www.jbc.org/ at Universiteitsbibliotheek Utrecht on December 3, 2015

Westerveld, A., Jaspers, N. G. J., Bootsma, D., and Hoeijmakers, J. H. J. (1996) Mutational analysis of the human nucleotide excision repair gene ERCC1. *Nucleic Acids Res.* **24,** 3370–3380
8. Sargent, R. G., Meservy, J. L., Perkins, B. D., Kilburn, A. E., Intody, Z., Adair, G. M., Nairn, R. S., and Wilson, J. H. (2000) Role of the nucleotide excision repair gene ERCC1 in formation of recombination-dependent rearrangements in mammalian cells. *Nucleic Acids Res.* **28,** 3771–3778
9. Al-Minawi, A. Z., Lee, Y.-F., Håkansson, D., Johansson, F., Lundin, C., Saleh-Gohari, N., Schultz, N., Jenssen, D., Bryant, H. E., Meuth, M., Hinz, J. M., and Helleday, T. (2009) The ERCC1/XPF endonuclease is required for completion of homologous recombination at DNA replication forks stalled by inter-strand cross-links. *Nucleic Acids Res.* **37,** 6400–6413
10. Niedernhofer, L. J., Odijk, H., Budzowska, M., van Drunen, E., Maas, A., Theil, A. F., de Wit, J., Jaspers, N. G. J., Beverloo, H. B., Hoeijmakers, J. H. J., and Kanaar, R. (2004) The structure-specific endonuclease Ercc1-Xpf is required to resolve DNA interstrand cross-link-induced double-strand breaks. *Mol. Cell Biol.* **24,** 5776–5787
11. Wu, Y., Mitchell, T. R. H., and Zhu, X.-D. (2008) Human XPF controls TRF2 and telomere length maintenance through distinctive mechanisms. *Mech. Ageing Dev.* **129,** 602–610
12. Muñoz, P., Blanco, R., Flores, J. M., and Blasco, M. A. (2005) XPF nuclease-dependent telomere loss and increased DNA damage in mice overexpressing TRF2 result in premature aging and cancer. *Nat. Genet.* **37,** 1063–1071
13. Zhu, X.-D., Niedernhofer, L., Kuster, B., Mann, M., Hoeijmakers, J. H. J., and de Lange, T. (2003) ERCC1/XPF removes the 3′overhang from uncapped telomeres and represses formation of telomeric DNA-containing double minute chromosomes. *Mol. Cell* **12,** 1489–1498
14. Ahmad, A., Robinson, A. R., Duensing, A., van Drunen, E., Beverloo, H. B., Weisberg, D. B., Hasty, P., Hoeijmakers, J. H. J., and Niedernhofer, L. J. (2008) ERCC1-XPF endonuclease facilitates DNA double-strand break repair. *Mol. Cell Biol.* **28,** 5082–5092
15. Al-Minawi, A. Z., Saleh-Gohari, N., and Helleday, T. (2008) The ERCC1/XPF endonuclease is required for efficient single-strand annealing and gene conversion in mammalian cells. *Nucleic Acids Res.* **36,** 1–9
16. de Laat, W. L., Sijbers, A. M., Odijk, H., Jaspers, N. G. J., and Hoeijmakers, J. H. J. (1998) Mapping of interaction domains between human repair proteins ERCC1 and XPF. *Nucleic Acids Res.* **26,** 4146–4152
17. de Laat, W. L., Jaspers, N. G. J., and Hoeijmakers, J. H. J. (1999) Molecular mechanism of nucleotide excision repair. *Genes Dev.* **13,** 768–785
18. Tripsianes, K., Folkers, G., Ab, E., Das, D., Odijk, H., Jaspers, N. G. J., Hoeijmakers, J. H. J., Kaptein, R., and Boelens, R. (2005) The structure of the human ERCC1/XPF interaction domains reveals a complementary role for the two proteins in nucleotide excision repair. *Structure* **13,** 1849–1858
19. Ciccia, A., McDonald, N., and West, S. C. (2008) Structural and functional relationships of the XPF/MUS81 family of proteins. *Annu. Rev. Biochem.* **77,** 259–287
20. Tripsianes, K., Folkers, G. E., Zheng, C., Das, D., Grinstead, J. S., Kaptein, R., and Boelens, R. (2007) Analysis of the XPA and ssDNA-binding surfaces on the central domain of human ERCC1 reveals evidence for subfunctionalization. *Nucleic Acids Res.* **35,** 5789–5798
21. Tsodikov, O. V., Enzlin, J. H., Schärer, O. D., and Ellenberger, T. (2005) Crystal structure and DNA binding functions of ERCC1, a subunit of the DNA structure-specific endonuclease XPF-ERCC1. *Proc. Natl. Acad. Sci. U.S.A.* **102,** 11236–11241
22. Das, D., Folkers, G. E., van Dijk, M., Jaspers, N. G. J., Hoeijmakers, J. H. J., Kaptein, R., and Boelens, R. (2012) The structure of the XPF-ssDNA complex underscores the distinct roles of the XPF and ERCC1 helix-hairpin-helix domains in ss/ds DNA recognition. *Structure* **20,** 667–675
23. Kondo, S., Mamada, A., Miyamoto, C., Keong, C.-H., Satoh, Y., and Fujiwara, Y. (1989) Late onset of skin cancers in 2 xeroderma pigmentosum group F siblings and a review of 30 Japanese xeroderma pigmentosum patients in groups D, E and F. *Photo-dermatology* **6,** 89–95
24. Sijbers, A. M., van Voorst Vader, P. C., Snoek, J. W., Raams, A., Jaspers, N. G. J., and Kleijer, W. J. (1998) Homozygous R788W point mutation in the XPF gene of a patient with xeroderma pigmentosum and late-onset neurologic disease. *J. Invest. Dermatol.* **110,** 832–836
25. Vermeulen, W., Rademakers, S., Jaspers, N. G. J., Appeldoorn, E., Raams, A., Klein, B., Kleijer, W. J., Kjærsgård Hansen, L., and Hoeijmakers, J. H. J. (2001) A temperature-sensitive disorder in basal transcription and DNA repair in humans. *Nat. Genet.* **27,** 299–303
26. Tian, M., Shinkura, R., Shinkura, N., and Alt, F. W. (2004) Growth retardation, early death, and DNA repair defects in mice deficient for the nucleotide excision repair enzyme XPF. *Mol. Cell Biol.* **24,** 1200–1205
27. Niedernhofer, L. J., Garinis, G. A., Raams, A., Lalai, A. S., Robinson, A. R., Appeldoorn, E., Odijk, H., Oostendorp, R., Ahmad, A., van Leeuwen, W., Theil, A. F., Vermeulen, W., van der Horst, G. T. J., Meinecke, P., Kleijer, W. J., Vijg, J., Jaspers, N. G. J., and Hoeijmakers, J. H. J. (2006) A new progeroid syndrome reveals that genotoxic stress suppresses the somatotroph axis. *Nature* **444,** 1038–1043
28. Kashiyama, K., Nakazawa, Y., Pilz, D. T., Guo, C., Shimada, M., Sasaki, K., Fawcett, H., Wing, J. F., Lewin, S. O., Carr, L., Li, T.-S., Yoshiura, K., Utani, A., Hirano, A., Yamashita, S., Greenblatt, D., Nardo, T., Stefanini, M., McGibbon, D., Sarkany, R., Fassihi, H., Takahashi, Y., Nagayama, Y., Mitsutake, N., Lehmann, A. R., and Ogi, T. (2013) Malfunction of nuclease ERCC1-XPF results in diverse clinical manifestations and causes Cockayne syndrome, xeroderma pigmentosum, and Fanconi anemia. *Am. J. Hum. Genet.* **92,** 807–819
29. Bogliolo, M., Schuster, B., Stoepker, C., Derkunt, B., Su, Y., Raams, A., Trujillo, J. P., Minguillón, J., Ramírez, M. J., Pujol, R., Casado, J. A., Baños, R., Rio, P., Knies, K., Zúñiga, S., Benítez, J., Bueren, J. A., Jaspers, N. G. J., Schärer, O. D., de Winter, J. P., Schindler, D., and Surrallés, J. (2013) Mutations in *ERCC4*, encoding the DNA-repair endonuclease XPF, cause Fanconi anemia. *Am. J. Hum. Genet.* **92,** 800–806
30. van Duin, M., van den Tol, J., Warmerdam, P., Odijk, H., Meijer, D., Westerveld, A., Bootsma, D., and Hoeijmakers, J. H. J. (1988) Evolution and mutagenesis of the mammalian excision repair gene ERCC-1. *Nucleic Acids Res.* **16,** 5305–5322
31. Jaspers, N. G. J., Raams, A., Silengo, M. C., Wijgers, N., Niedernhofer, L. J., Robinson, A. R., Giglia-Mari, G., Hoogstraten, D., Kleijer, W. J., Hoeijmakers, J. H. J., and Vermeulen, W. (2007) First reported patient with human ERCC1 deficiency has cerebro-oculo-facio-skeletal syndrome with a mild defect in nucleotide excision repair and severe developmental failure. *Am. J. Hum. Genet.* **80,** 457–466
32. Gregg, S. Q., Robinson, A. R., and Niedernhofer, L. J. (2011) Physiological consequences of defects in ERCC1-XPF DNA repair endonuclease. *DNA Repair* **10,** 781–791
33. McWhir, J., Selfridge, J., Harrison, D. J., Squires, S., and Melton, D. W. (1993) Mice with DNA repair gene (ERCC-1) deficiency have elevated levels of p53, liver nuclear abnormalities and die before weaning. *Nat. Genet.* **5,** 217–224
34. Imoto, K., Boyle, J., Oh, K., Khan, S., Ueda, T., Nadem, C., Slor, H., Orgal, S., Gadoth, N., Busch, D., Jaspers, N. G. J., Tamura, D., DiGiovanna, J. J., and Kraemer, K. H. (2007) Patients with defects in the interacting nucleotide excision repair proteins ERCC1 or XPF show xeroderma pigmentosum with late onset severe neurological degeneration. *J. Invest. Dermatol.* **127,** Suppl S92
35. Farabaugh, P. J. (1978) Sequence of the lacI gene. *Nature* **274,** 765–769
36. Blattner, F. R., Plunkett, G., 3rd, Bloch, C. A., Perna, N. T., Burland, V., Riley, M., Collado-Vides, J., Glasner, J. D., Rode, C. K., Mayhew, G. F., Gregor, J., Davis, N. W., Kirkpatrick, H. A., Goeden, M. A., Rose, D. J., Mau, B., and Shao, Y. (1997) The complete genome sequence of *Escherichia coli* K-12. *Science* **277,** 1453–1462
37. Nieba, L., Nieba-Axmann, S. E., Persson, A., Hämäläinen, M., Edebratt, F., Hansson, A., Lidholm, J., Magnusson, K., Karlsson, A. F., and Plückthun, A. (1997) BIACORE analysis of histidine-tagged proteins using a chelating NTA sensor chip. *Analytical Biochemistry* **252,** 217–228
38. Das, D., Tripsianes, K., Jaspers, N. G. J., Hoeijmakers, J. H. J., Kaptein, R., Boelens, R., and Folkers, G. E. (2008) The HhH domain of the human DNA repair protein XPF forms stable homodimers. *Proteins* **70,** 1551–1563
39. Politou, A. S., Thomas, D. J., and Pastore, A. (1995) The folding and stability of titin immunoglobulin-like modules, with implications for the mechanism of elasticity. *Biophys. J.* **69,** 2601–2610
40. Ericsson, U. B., Hallberg, B. M., Detitta, G. T., Dekker, N., and Nordlund, P. (2006) Thermofluor-based high-throughput stability optimization of

Downloaded from http://www.jbc.org/ at Universiteitsbibliotheek Utrecht on December 3, 2015

proteins for structural studies. *Anal. Biochem.* **357,** 289–298
41. Cavanagh J., Fairbrother, W. J., Palmer G. A., Rance, M., and Skelton J. N. (2007) *Protein NMR Spectroscopy,* 2nd Ed., pp. 533–678, Academic Press, Inc., San Diego, CA
42. Sattler, M., Schleucher, J., and Griesinger, C. (1999) Heteronuclear multidimensional NMR experiments for the structure determination of proteins in solution employing pulsed field gradients. *Prog. NMR Spectrosc.* **34,** 93–158
43. Delaglio, F., Grzesiek, S., Vuister, G. W., Zhu, G., Pfeifer, J., and Bax, A. (1995) NMRPipe: a multidimensional spectral processing system based on UNIX pipes. *J. Biomol. NMR* **6,** 277–293
44. Goddard, T. D., and Kneller, D. G. (2006) *SPARKY 3*, version 3.113, University of California, San Francisco
45. Baxter, N. J., and Williamson, M. P. (1997) Temperature dependence of ^{1}H chemical shifts in proteins. *J. Biomol. NMR* **9,** 359–369
46. Cierpicki, T., and Otlewski, J. (2001) Amide proton temperature coefficients as hydrogen bond indicators in proteins. *J. Biomol. NMR* **21,** 249–261
47. Englander, S. W., and Kallenbach, N. R. (1983) Hydrogen exchange and structural dynamics of proteins and nucleic acids. *Q. Rev. Biophys.* **16,** 521–655
48. Bai, Y., Milne, J. S., Mayne, L., and Englander, S. W. (1993) Primary structure effects on peptide group hydrogen exchange. *Proteins* **17,** 75–86
49. Hwang, T.-L., van Zijl, P. C. M., and Mori, S. (1998) Accurate quantitation of water-amide proton exchange rates using the phase-modulated CLEAN chemical EXchange (CLEANEX-PM) approach with a Fast-HSQC (FHSQC) detection scheme. *J. Biomol. NMR* **11,** 221–226
50. Güntert, P. (2009) Automated structure determination from NMR spectra. *Eur. Biophys. J.* **38,** 129–143
51. Güntert, P., Mumenthaler, C., and Wüthrich, K. (1997) Torsion angle dynamics for NMR structure calculation with the new program DYANA. *J. Mol. Biol.* **273,** 283–298
52. Shen, Y., Delaglio, F., Cornilescu, G., and Bax, A. (2009) TALOS+: a hybrid method for predicting protein backbone torsion angles from NMR chemical shifts. *J. Biomol. NMR* **44,** 213–223
53. Cornilescu, G., Delaglio, F., and Bax, A. (1999) Protein backbone angle restraints from searching a database for chemical shift and sequence homology. *J. Biomol. NMR* **13,** 289–302
54. Brünger, A. T., Adams, P. D., Clore, G. M., DeLano, W. L., Gros, P., Grosse-Kunstleve, R. W., Jiang, J.-S., Kuszewski, J., Nilges, M., Pannu, N. S., Read, R. J., Rice, L. M., Simonson, T., and Warren, G. L. (1998) Crystallography & NMR system: a new software suite for macromolecular structure determination. *Acta Crystallogr. D Biol. Crystallogr.* **54,** 905–921
55. Nederveen, A. J., Doreleijers, J. F., Vranken, W., Miller, Z., Spronk, C. A., Nabuurs, S. B., Güntert, P., Livny, M., Markley, J. L., Nilges, M., Ulrich, E. L., Kaptein, R., and Bonvin, A. M. J. J. (2005) RECOORD: a recalculated coordinate database of 500+ proteins from the PDB using restraints from the BioMagResBank. *Proteins* **59,** 662–672
56. Vriend, G. (1990) WHAT IF: a molecular modeling and drug design program. *J. Mol. Graph.* **8,** 52–56
57. Hooft, R. W., Vriend, G., Sander, C., and Abola, E. E. (1996) Errors in protein structures. *Nature* **381,** 272–272
58. Doreleijers, J. F., Sousa da Silva, A. W., Krieger, E., Nabuurs, S. B., Spronk, C. A., Stevens, T. J., Vranken, W. F., Vriend, G., and Vuister, G. W. (2012) CING: an integrated residue-based structure validation program suite. *J. Biomol. NMR* **54,** 267–283
59. DeLano, W. L. (2012) *The PyMOL Molecular Graphics System*, version 1.5.0.1, Schroedinger, LLC, New York
60. Koradi, R., Billeter, M., and Wüthrich, K. (1996) MOLMOL: a program for display and analysis of macromolecular structures. *J. Mol. Graph.* **14,** 51–55
61. Chen, Y.-H., Yang, J. T., and Chau, K. H. (1974) Determination of the helix and beta form of proteins in aqueous solution by circular dichroism. *Biochemistry* **13,** 3350–3359
62. McDonnell, J. M. (2001) Surface plasmon resonance: towards an understanding of the mechanisms of biological molecular recognition. *Curr. Opin. Chem. Biol.* **5,** 572–577
63. Purich, D. L., and Allison, R. D. (1980) Isotope exchange methods for elucidating enzymic catalysis. *Methods Enzymol.* **64,** 3–46
64. Chelli, R., Gervasio, F. L., Procacci, P., and Schettino, V. (2002) Stacking and T-shape competition in aromatic-aromatic amino acid interactions. *J. Am. Chem. Soc.* **124,** 6133–6143
65. Serdyuk, I. N., Zaccai, N. R., and Zaccai, J. (2007) *Methods in Molecular Biophysics: Structure, Dynamics, Function*, pp. 21–37, Cambridge University Press, Cambridge, UK
66. Finkelstein, A. V., and Ptitsyn, O. B. (2002) *Protein Physics: A Course of Lectures*, pp. 57–72 and 117–123, Academic Press, Inc., San Diego

Downloaded from http://www.jbc.org/ at Universiteitsbibliotheek Utrecht on December 3, 2015

jbc The Journal of Biological Chemistry
AFFINITY SITES
ASBMB American Society for Biochemistry and Molecular Biology

DNA and Chromosomes:

The Cerebro-oculo-facio-skeletal Syndrome Point Mutation F231L in the ERCC1 DNA Repair Protein Causes Dissociation of the ERCC1-XPF Complex

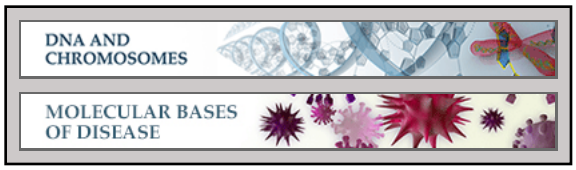

Maryam Faridounnia, Hans Wienk, Lidija Kovacic, Gert E. Folkers, Nicolaas G. J. Jaspers, Robert Kaptein, Jan H. J. Hoeijmakers and Rolf Boelens

J. Biol. Chem. 2015, 290:20541-20555.
doi: 10.1074/jbc.M114.635169 originally published online June 17, 2015

Access the most updated version of this article at doi: 10.1074/jbc.M114.635169

Find articles, minireviews, Reflections and Classics on similar topics on the JBC Affinity Sites.

Alerts:
- When this article is cited
- When a correction for this article is posted

Click here to choose from all of JBC's e-mail alerts

This article cites 59 references, 14 of which can be accessed free at
http://www.jbc.org/content/290/33/20541.full.html#ref-list-1

Downloaded from http://www.jbc.org/ at Universiteitsbibliotheek Utrecht on December 3, 2015